Article:
Silva, D, Piazolo, S and Daczko, NR (2022) Trapped K-feldspar phenocrysts as a signature of melt migration pathways within active high-strain zones. Journal of Metamorphic Geology. ISSN: 0263-4929

https://doi.org/10.1111/jmg.12698

Trapped K-feldspar phenocrysts as a signature of melt migration pathways within active high-strain zones

David Silva[a,b], Sandra Piazolo[a,c], Nathan R. Daczko[a]

[a] ARC Centre of Excellence for Core to Crust Fluid Systems and GEMOC, School of Natural Sciences, Macquarie University, NSW 2109, Australia

[b] Department of Earth, Ocean and Atmospheric Sciences, University of British Columbia, Vancouver, BC V6T 1Z4, Canada

[c] School of Earth and Environment, Institute of Geophysics and Tectonics, University of Leeds, Leeds, LS2 9JT, United Kingdom

Corresponding author: David Silva (david.barbosa-da-silva@students.mq.edu.au)

Keywords: High-strain zone; Metasomatism; Melt extraction; Collapse structures; Phenocrysts.

ABSTRACT

Melt migration through high-strain zones in the crust fundamentally influences their rheological behaviour and is important for the transfer of fluids to upper crustal regions. The inference of former melt-present deformation, based on field observations, may be hampered if the high-strain zone experience a low time-integrated melt flux or high melt volume expulsion during deformation. In these cases, typical macro-scale field evidence of former melt presence limits interpretations. In this contribution, we investigate igneous field evidence ranging from obvious to cryptic in the Gough Dam shear zone (central Australia), a 2–4 km wide high-strain zone shown to have acted as a significant melt pathway during the Alice Springs Orogeny. Within bands of the high-strain zone, granitic lenses are easily discernible in the field and are inferred to have formed during melt present

deformation. Related coarse K-feldspar is observed in biotite-rich (> 75 vol%) schist (glimmerite) as either isolated grains, forming trails (sub)parallel to the main foliation, or in aggregates with subordinate quartz. Detailed characterisation of the granitic lenses shows that pockets of phenocrysts may be entrained in the shear zone. If melt expulsion and melt-rock interaction is severe, isolated K-feldspar grains in glimmerite may form. These grains exhibit (i) partially preserved crystal faces; (ii) a lack of internal grain deformation; (iii) reaction textures preferentially formed along the main crystallographic axes showing dissolution of K-feldspar and precipitation of dominantly biotite; (iv) low-strain domains between multiple K-feldspar grains are inferred to enclose crystallised melt pockets, with some apparently isolated grains showing connectivity in three dimensions; and (v) a weak quartz and K-feldspar crystallographic preferred orientation. These observations suggest an igneous phenocrystic origin for the isolated K-feldspar grains hosted in glimmerite which is consistent with the observed REE concentration patterns with positive Eu anomaly. We propose that the K-feldspar phenocrysts are early-formed crystals that were entrained into the glimmerite rocks as reactive melt migrated through the actively deformating high-strain zone. Previously entrained K-feldspar phenocrysts were trapped during the collapse of the melt pathway when melt flux-related fluid pressure waned while confining pressure and tectonic stress were still significant. The active deformation facilitated expulsion or loss of the melt phase but retainment and trapping of phenocrysts. Hence, the presence of isolated or "trains" of K-feldspar phenocrysts are a cryptic signature of syndeformational melt transfer. If melt transfer occurs in an open chemical system, phenocrysts will be entrained within the reaction product of melt rock interaction. We suggest that these so-called "trapped phenocrysts" are a viable indicator of former syntectonic melt passage through rocks.

1. INTRODUCTION

High-strain zones are important crustal-scale conduits for melt transfer from regions of melt production (lower- to middle-crust) to shallower crustal depths, significantly contributing to the observed segregation of highly silicic melt towards the upper crust (Hollister & Crawford, 1986;

Hutton, 1988; D'lemos *et al.,* 1992; Brown, 1994; Vigneresse, 1995; Weinberg *et al.,* 2004; Brown & Rushmer, 2006; Etheridge *et al.*, 2020). Furthermore, the former presence of melt in highly strained rocks suggests a high-strain zone with very weak rheology, and by consequence increased strain localisation in such zones compared to the surrounding consolidated rocks (Rosenberg & Handy, 2005; Levine *et al.,* 2013; Searle, 2013; Lee *et al.,* 2018; Daczko & Piazolo, 2022). Whilst melt-present high-strain zones preserve signatures of the former presence of melt (e.g., granitic lenses), not all melt-present high-strain zones may show such clear signatures of former magmatic activity. The recognition of such zones is difficult if they preserve low crystallised melt volumes due to limited presence of macroscopic crystallised igneous material (i.e., leucosome) arranged in seams, pockets or dykes in the deformed rock (e.g., Weinberg *et al.,* 2013; Stuart *et al.,* 2017, 2018; Daczko & Piazolo, 2022). However, low percentages of preserved crystallised melt volume are expected if deformation is synchronous with melt presence, as deformation will markedly enhance movement of melt (Van der Molen & Paterson, 1979; Rosenberg & Handy, 2005; Brown & Solar, 1998; Collins & Sawyer, 1996; Etheridge *et al.*, 2020). Therefore, the signature of the former presence of melt in high-strain zones may be cryptic at the outcrop scale and requires in-depth microstructural analysis to identify it (Daczko & Piazolo, 2022). For example, microstructures may include small mono- or multiphase pockets at triple points and/or elongated interstitial grains (Beere, 1975; Von Bargen & Waff, 1986; Holness & Sawyer, 2008; Závada *et al.,* 2007; Stuart *et al.,* 2017, 2018; Lee *et al.,* 2018). In addition, if the melt was chemically reactive at the time of deformation, a change in mineral assemblage and bulk composition of the zone also occurs (e.g., Daczko *et al*., 2016; Stuart *et al*., 2018; Meek *et al*., 2019; Piazolo *et al*., 2020). If melt fractions where locally high (>> 10 vol%), areas that were occupied by melt before expulsion, develop so-called "collapse structures" which are most easily recognised if the channelised melt network was at a high angle to the general rock foliation (e.g., Bons, 1999; Marchildon & Brown, 2003; Druguet & Carreras, 2006; Diener *et al*., 2014; Wolfram *et al*., 2017).

In summary, it is difficult to recognise in the field the former presence of melt in highly strained rocks if deformation was synchronous with melt presence. However, failure to recognise former melt presence, may lead to erroneous interpretations of high-strain rocks in terms of their rheology at the time of deformation, based on the difficulty of quantifying the former melt volume fraction, along with inaccurate interpretations of the strain history and even incorrect identification of the rock type (Bons, 1999; Kriegsman, 2001; Brown, 2005; Bons *et al.,* 2008, 2009). Thus, the recognition of potentially cryptic signatures of the former presence of melt in high-strain rocks is crucial to interpret and understand melt migration through the lithosphere, as well as to develop a thorough understanding of the tectonic and magmatic history of an area, including periods of significant melt transfer.

To establish what field signatures can be used to recognise former syntectonic melt presence, it is necessary to develop an understanding of how igneous components may be preserved despite syntectonic melt flux and expulsion. In this contribution, we present a detailed microstructural study of rocks present in the 2–4 km-wide Gough Dam shear zone that was active during the Alice Springs Orogeny (ASO) in central Australia, which has been shown to have deformed in the presence of melt (Piazolo *et al.,* 2020; Silva *et al.,* 2022). This high-strain zone is characterised by highly strained, biotite-dominated schist (glimmerite schist) formed by melt-mediated metasomatic reaction with a granulite precursor rock (Silva *et al.,* 2022). To advance our ability to recognise formerly melt-present high-strain zones, we investigate the microstructural signature of samples with obvious igneous components and samples lacking these clear field signatures. Chosen samples span from granitic lenses to isolated grains or trains of mm-scale faceted K-feldspar immersed in the glimmerite *sensu stricto* (*s.s.*). Granitic lenses occur with or without selvedges and are inferred from previous studies to represent lenses of magma frozen in the high-strain zone (Piazolo *et al*., 2020).

Here, we use quantitative orientation mapping, scanning electron microscope (SEM) based imaging and chemical analysis to characterise quartz and K-feldspar microstructures. Results show that for both granitic lenses and glimmerite samples, the microstructural characteristics are not

typical for high-strain rocks deformed by solid-state deformation dominated by dislocation creep. The solid igneous minerals such as coarse, K-feldspar grains remain largely undeformed, as the present melt accommodates most strain and effectively "shields" the solid grains. Based on our results, we suggest that K-feldspar phenocrysts within a product of melt-rock interaction, e.g., a glimmerite schist, may be used as an additional indicator for the recognition of former melt flux in high-strain zones. We interpret their presence in highly metasomatised rocks as a consequence of early feldspar crystallisation in a syntectonic melt, succeeded by the structural collapse of the adjacent rocks during melt expulsion, resulting in K-feldspar entrapment in the biotite dominated schist. As such "trapped phenocrysts" may be used to delineate former pathways of melt migrating through high-strain zones from deeper crustal origins.

2. GENERAL GEOLOGICAL BACKGROUND

The study area is in the Arunta Region, central Australia, which was most recently deformed in the ASO, a ~700 km long by ~80 km wide intracontinental orogeny that spanned the period of 450 to 300 Ma (Collins & Teyssier, 1989; Hand & Sandiford, 1999; Mawby *et al.,* 1999; Scrimgeour, 2013; Fig. 1). An extensive regional system of anastomosing high-strain zones and localised deep crustal thrust faults are present, and these cuts most of the high-grade metamorphic complexes in the region, with peak *P-T* conditions of 5.0–6.5 kbar and 500°–600° C in the west and central parts of the orogen (Cartwright *et al.,* 1999; Ballèvre *et al.,* 2000; Raimondo *et al.,* 2011, 2014; Fig. 1). Crustal thickening with an estimated ~100 km of horizontal shortening occurred during tectonic N-S compression and involved the exhumation of granulitic basement rocks (Shaw *et al.,* 1984; Teyssier, 1985; Collins & Teyssier, 1989). Crustal shortening during the ASO induced intense and large-scale crustal denudation of metamorphic and igneous terranes, with deposition of multiple synorogenic sedimentary sequences up to 4km in thickness in basins surrounding the Arunta Region (Haines *et al.*, 2001; Raimondo *et al.,* 2014). Multiple episodes of pegmatite intrusions in the Arunta Region took place throughout the duration of the ASO and their ages correlate with the temporal

129 formation of regional structures and deposition of synorogenic sedimentary sequences in the adjacent
130 basins (Buick *et al.,* 2008; Varga *et al.,* 2022). The lack of ASO-aged partial melting of the basement
131 rocks suggests a deep-seated parental melt source for the exposed ASO-aged igneous rocks, which
132 comprise mainly pegmatite dykes and minor granite plutons (Buick *et al.,* 2008; Piazolo *et al.,* 2020).
133 Tectonic compression was enhanced during periods of extension in the Tasmanides Orogeny,
134 adjacent to the Eastern Australian plate boundary (Raimondo *et al.,* 2014; Silva *et al.,* 2018). The
135 study area lies in the Strangways Metamorphic Complex (SMC) formed during the Strangways Event
136 (*c*. 1735–1690 Ma; Fig. 1). The SMC is cut by steeply dipping, km-wide, hydrous and multi-
137 reactivated high-strain zones that were formed during the ASO (Fig. 1). These comprise upper
138 amphibolite- to greenschist-facies schist belts that include layers of K-feldspar-biotite-quartz schist
139 (i.e., 40–60 vol% mica; identified hereafter as glimmerite schist) and glimmerite *sensu stricto* (*s.s*)
140 (i.e., > 75 vol% mica with very low proportions of quartz).

141 Granitic lenses with and without glimmerite selvedges and glimmerite schist were
142 sampled from the Gough Dam shear zone (GDSZ), a E-W to NNW-SSE trending, 2–4 km-wide,
143 steeply dipping (60°–90° towards N) high-strain zone (Fig. 1). Based on shear band orientations and
144 sigma clast kinematic indicators, the GDSZ represents a S-directed reverse high-strain zone that
145 juxtaposed the northern SMC with the Harts Range Metamorphic Complex (HRMC) (Collins &
146 Shaw, 1995; Bendall, 2000; Fig. 1). This high-strain zone is characterised by metasomatic hydration
147 of the bi-modal interlayered anhydrous mafic-felsic granulites, quartzo-feldspathic gneisses, minor
148 calcsilicate and amphibolite rocks constituting the Palaeoproterozoic SMC basement of the Arunta
149 Region (Piazolo *et al.,* 2020; Silva *et al.,* 2022). The formation of glimmerite schist in the GDSZ and
150 glimmerite selvedges observed around granitic lenses was recently proposed by Silva *et al.* (2022) as
151 involving multiple periods of migration of extensive volumes of hydrous peraluminous melt through
152 the high-strain zone during the ASO. Reaction of the migrating melts with the precursor quartzo-
153 feldspathic granulite rocks was inferred within mainly channelised pathways parallel to the high-
154 strain zone foliation. The magnitude of melt needed to drive the melt-mediated reaction forming

155 glimmerite and the size and longitudinal continuity of field indicators of former melt flux increases
156 towards the centre of the GDSZ (Silva *et al.*, 2022). Recent research on the nearby Cattle Water Pass
157 shear zone also demonstrated that melt-rock interaction and migration of significant volumes of melt
158 through high-strain zones was important in enriching the rocks in oxide minerals such as ilmenite
159 (Ghatak *et al.*, 2022).
160
161 **2.1. Field relationships**
162 The main rock types present in the GDSZ schist belt are phyllonitic biotite-rich
163 quartzo-feldspathic gneiss (hereafter named granitic gneiss), felsic and mafic granulite pods, quartz-
164 rich rafts, and sparse cm-wide garnet-bearing granulites; the high-strain rocks contain biotite,
165 sillimanite, and rare kyanite, delineating the steep north-plunging lineation (Ballèvre *et al.,* 1997).
166 Continuous cm- to dm-scale banding parallel to the GDSZ foliation is observed in the study area and
167 these span compositions ranging from granitic (i.e., near-euhedral Kfs ± qz and subordinate
168 plagioclase and biotite (< 5 vol%); Fig. 2a) to glimmerite bands of high biotite content (up to 80
169 vol%; Fig. 2b). Small lenses of variably deformed granite resembling pinch-and-swell structures are
170 observed, creating isolated lenses of granite elongate along the foliation. These granite trails usually
171 display mm-width biotite-rich (> 50 vol%) selvedges (Fig. 2a, c, d). Quartz-rich rafts (i.e., quartzite
172 mylonite; Fig. 2h) embedded in glimmerite schist form bodies of more than 10 m in length and up to
173 50 cm in width. The study site is dominated by metre-scale layers of glimmerite schist (Fig. 2b)
174 composed of a matrix of dominantly biotite (~50 vol%) with up to ~30 vol% of quartz, muscovite
175 (~10 vol%) and sillimanite (~1 vol%), with isolated or clustered, coarse (up to 2–3 cm across) near-
176 euhedral K-feldspar making up the remaining mineralogical fraction (up to 30 vol%; Fig. 2e–g). The
177 latter form discontinuous trails along the foliation (Fig. 2a, b, e–g). The glimmerite component is
178 observed to partially replace and disaggregate quartzite mylonite rafts along fractures (black and
179 white arrow; Fig. 2h) (Silva *et al.,* 2022). Similar rock modification to glimmerite is observed in a
180 range of rock types including felsic granulite and granitic gneiss (Fig. 2a–d).

3. METHOD OF ANALYSIS

3.1. Petrography and quantitative orientation analysis

Sample mineral observations were made on polished thin sections cut in the structural XZ plane using a petrographic microscope, the Virtual Petrographic Microscope (Tetley & Daczko, 2014) and ImageJ 1.47v (Rasband, 1997–2018). Mineral abbreviations follow Whitney & Evans (2010). Microstructural/crystallographic characterisation of thin sections was performed using a FEI Quanta 650 FEG-ESEM with AZtec software and an Oxford/HKL Nordlys S EBSD system at the University of Leeds, UK. EBSD mapping was performed, covering a large area of the thin section and small individual maps in specific regions of the sample, recording the mineral EDS spectra along with the EBSD data. Working conditions were: 20 kV accelerating voltage, 20–26 mm working distance, 70° specimen tilt and step size between 6 and 12 μm depending on the area covered and grain size. Automatic indexation was performed using AZtec software (Oxford Instruments). HKL Channel 5 and AZtecCrystal software (Oxford Instruments) were used to execute standard noise reduction and to extrapolate missing data using at least and in succession 8, 7, 6 and finally 5 identical neighbours with similar orientation. Grain orientation maps using Euler angles and an inverse pole figure (IPF) colour coding were generated using MTEX and HKL Channel 5 software (Bachmann *et al.,* 2010; Henry *et al.,* 2017; Henry, 2018). Presented maps include grain boundaries, defined as a boundary with a misorientation above 10°, and dauphine twin boundaries for quartz, defined as a 60° misorientation around the c-axis. The presence and character of crystallographic preferred orientation (CPO) of quartz and K-feldspar was assessed using pole figures plotted on the lower hemisphere with one point per grain. To quantify the intensity of the CPO, J-index (i.e., second-moment distribution of discrete crystal orientation data in Euler angle space (Bunge, 2013)) and M-index (i.e., distribution of uncorrelated misorientation angles (Skemer *et al.,* 2005)) are presented. Grain internal deformation is assessed by plotting the change in crystallographic orientation relative to a reference orientation.

206 In should be noted, that the majority of the non-indexed sectors in EBSD maps (black regions) are
207 dominated by non-indexed biotite and lesser muscovite, as informed by petrographic microscopy.
208
209 **3.2. Imaging and geochemical analysis**
210 *Micro X-ray Fluorescence (μ-XRF)* analysis of the polished thin sections was used for
211 mineral identification, spatial distribution mapping and quantification of modal proportions. μ-XRF
212 analyses were performed using the Bruker M4 Tornado spectrometer at Macquarie University
213 Geoanalytical (MQGA), Sydney, Australia. The μ-XRF analyses were run with a tube voltage of
214 50 kV, a beam current of 200 μA, a chamber pressure of 20 mbar, an acquisition time of 15 ms/pixel
215 and using a step size of 25 μm. AMICS (Advanced Mineral Identification and Characterization
216 System) was used to convert the X-ray fluorescence spectra to produce detailed mineral maps.
217 *Backscatter Electron (BSE)* images and *associated EDS point analyses* were used for
218 both mineral identification and imaging of microstructures. Polished thin sections were carbon-coated
219 and imaged in a Hitachi Desktop Scanning Electron Microscope (SEM) at the OptoFab node of the
220 Australian National Fabrication Facility, Macquarie University, Sydney, Australia. The operating
221 conditions of the SEM were low vacuum and 15 kV accelerating voltage. A large area BSE scan of
222 the thin section was performed using the FEI 650 ESEM at the University of Tasmania, Australia, at
223 low vacuum and 20 kV accelerating voltage.
224 *Electron microprobe analyses* (EMPA) acquired compositional data of silicates using
225 a JEOL JXA 8530F Plus field emission electron microprobe at the Central Science Laboratory,
226 University of Tasmania. The instrument is equipped with a field emission source, running an
227 accelerating voltage of 15 kV, a beam current of 15 nA and a beam size of 10 μm. The instrument
228 has 5 wavelength dispersive spectrometers and is operated using the Probe Software Inc. "Probe For
229 EPMA" software package. Plagioclase Lake County, Hornblende Kakanui, Augite Kakanui, Pyrope
230 Kakanui, Olivine Springwater, Garnet Roberts Victor Mine (all Smithsonian; Jarosewich *et al.,* 1980)
231 and Orthoclase from P&H Developments UK were analysed as secondary standards to confirm the

quality of the analysis of the unknown material. A time-dependent intensity correction was applied on Na and K if applicable. Oxygen was calculated by cation stoichiometry and included in the matrix correction. Hydrogen was calculated based on the mineral formula and included in the matrix correction as well. The matrix correction algorithm utilised was Armstrong/Love Scott (Armstrong, 1988) and the mass absorption coefficients dataset was LINEMU < 10 keV (Henke, 1985) and CITZMU > 10 keV (Heinrich, 1966). Recalculated formulae for biotite and feldspar were made based on 22 and 16 oxygens, respectively (Table 1).

Laser Ablation Inductively Coupled Plasma Mass Spectrometry (LA-ICP-MS) was used to collect data for concentration of rare earth elements in K-feldspar in thin section using a Teledyne Analyte Excite 193 nm excimer laser coupled to an 7700x ICP-MS housed at Macquarie University Geoanalytical (MQGA), Sydney, Australia. Data was collected from thin sections using 60 seconds ablation at 10 Hz, 5 J/cm^2 fluence and spot size of 150 μm. Silicon (measured by EMP) was used as an internal standard for all minerals, and NIST 610 and 612, and basalt from the Columbia River (BCR-2) were used as external standards. The raw data signal was reduced using the GLITTER software (Griffin *et al.,* 2008).

Biotite thermometry

Temperature conditions for each sample are estimated using the titanium-in-biotite thermometer of Henry *et al.* (2005). The geothermometer is based on the titanium atoms per formula unit (Ti a.p.f.u.) composition of biotite in a peraluminous metapelite with Ti-bearing minerals (ilmenite or rutile) and graphite in the mineral assemblage, equilibrated at 4–6 kbar. Temperature estimates are made by using the concentration of Ti, Fe and Mg a.p.f.u. in biotite present in a glimmerite schist sample (Table 1). Taking the experimental conditions for the geothermometer (Henry *et al.,* 2005) into account, the expected accuracy of the temperature estimates is around ± 50°C and represent minimum temperatures based on the absence of graphite and accessory Ti-bearing minerals in the studied samples (Fig. S1).

4. RESULTS

4.1. Rationale for sample selection and analyses

Since we are specifically interested in identifying cryptic signatures, we investigated samples for the chemical and microstructural evidence "left behind" during the passage of melt. We selected two representative samples exhibiting direct field evidence of melt passage through granitic gneiss (i.e., gneiss containing granitic lenses; Fig. 2a, c, d; coordinates 23.14523°S, 134.56708°E, WGS84). The samples either have mm-wide biotite selvedges (GD1617; Fig. 3a, right sample) or a lack thereof (GD1620A; Fig. 3a, left sample) at the interface of lens to granitic gneiss. For the cryptic evidence of former melt presence, we investigated a representative glimmerite schist sample (sample GD1606) with enclosed coarse K-feldspar grains (Fig. 2b, e–g; coordinates 23.14694°S, 134.56517°E, WGS84). Characterisation of the mineral chemical composition and microstructure of mainly quartz and K-feldspar was performed to resolve the geochemical and deformation processes involved in the formation of the granitic lenses and the origin of K-feldspar grains enclosed in glimmerite.

4.2. General sample description

4.2.1. Granitic lenses

Granitic lenses from samples GD1620A and GD1617 feature a high vol% of interlocked K-feldspar grains (> 75%) with apparent subhedral habit and dimensions of 3–4 mm (GD1620A) and 1–3 mm (GD1617), and interstitial quartz grains of varied dimensions (Fig. 3). Thin interstitial grain boundary films of quartz and plagioclase are observed between coarse K-feldspar grains in sample GD1620A (Fig. 3c). The minor development of sub-grains in quartz and microcline with cross-hatched crystal twinning in K-feldspar is observed in both samples (Fig. 3b, c, e). In the modified granitic gneiss, biotite grains show a gradual increase in parallel orientation towards the contact to the granitic lens (Fig. 3b). This contrasts with the cm-scale glimmerite selvedge of sample GD1617, were biotite exhibits a strong shape and crystallographic preferred orientation (Fig. 3e).

Biotite grains lack typical solid-state internal deformation microstructures (e.g., kinking or folding, recrystallisation; black and white arrows in Fig. 3e). Biotite grains protrude into relict quartz grains forming embayments (Fig. 3e). Quartz grains form low apparent dihedral angles between two biotite grains and appear as thin interstitial bands in both samples (Fig. 3d, e).

4.2.2. Glimmerite with K-feldspar grains

The glimmerite schist is characterised by three main grain sizes, with the matrix dominated by fine-grained biotite (Bt; ~50 vol% of matrix), medium-grained quartz (Qz; ~30 vol% of matrix) and muscovite (Ms; ~10vol% of matrix), and interspersed coarse-grained K-feldspar grains (Kfs; ~30 vol% of sample) (Fig. 4a, d). The remaining glimmerite schist matrix is constituted by sillimanite (Sil; ~1 vol%) and ~9 vol% of a very fine-grained Al-Si-rich alteration product after aluminosilicates, mainly sillimanite and feldspars, and inferred to be kaolinite or pyrophyllite associated with late-stage local retrogression (labelled on as Alt. on figures), that fills grain micro-fractures (Fig. 4a, d, e). Small and minor plagioclase grains show preferential spatial arrangement near to and/or in contact with K-feldspar grains as small rims and occasionally in thin embayments (Fig. 5a, b). Due to the presence of the latter alteration product, we note that in the pre-alteration rock, the mode of sillimanite may have been higher, and plagioclase may have comprised a significant proportion of the assemblage. Minor proportions (< 1 vol%) of magnetite (~0.04 vol%), apatite (~0.017 vol%), monazite (~0.015 vol%) and zircon (~0.014 vol%) are observed in the matrix which is otherwise dominated by biotite and quartz.

The minerals in the rocks exhibit a strong shape preferred orientation, where coarse K-feldspar grains, biotite grains and bands of quartz grains are aligned parallel to the main lineation and lie in the foliation (S-plane; Berthé *et al.,* 1979) of the rock (Fig. 4a, b). Bands of quartz grains and biotite are not only seen parallel to the glimmerite schist foliation but may also form bands oriented at 45° relative to the foliation (C'-type shear bands; Berthé *et al.,* 1979) (Fig. 4a, b). Similar to the biotite grains in the selvedges from sample GD1617, biotite grains lack kinking, folding or

recrystallisation microstructures (Figs. 4b, c, and 5e, f). The coarse K-feldspar grains show (i) little evidence of crystal-plastic deformation (i.e., lack undulose extinction; Fig. 4a–c), (ii) apparent subhedral shape (i.e., semi-straight crystal faces; Fig. 4a–e), (iii) lack recrystallisation around the grain edges (i.e., lack core-mantle microstructure common in high-strain mylonite; Fig. 4e), and (iv) display fractures filled by fine-grained Al-Si-rich alteration product (Fig. 4e). Most coarse K-feldspar grains exhibit quartz inclusions (Fig. 4d, e), with plagioclase being less common (Fig. 5a) and one coarse K-feldspar grain shows a monazite inclusion (Fig. 4e). Biotite, sillimanite, and small quartz grains are observed to wrap around and form tails of matrix minerals at the extremities of the coarse K-feldspar and muscovite grains (Figs. 4e and 5c–e). Agglomerates of smaller quartz and feldspar grains, together with minor biotite, are visible in areas between the aligned coarse K-feldspar grains (i.e., in the strain shadows; Figs. 4d, e and 5b). The agglomerates of quartz and K-feldspar are irregularly-shaped and interstitial to the coarse K-feldspar (Figs. 4e and 5b). These small K-feldspar and quartz grains lack evidence for significant crystal-plastic deformation, i.e., they lack undulose extinction, subgrains and recrystallised grains (Figs. 4e and 5b).

4.3. Mineral chemistry

In the feldspar solid solution ternary plot (Fig. 6), the coarse K-feldspar grains present within glimmerite schist show a slightly variable composition within the 80–90 mol% orthoclase range. Analyses performed at the rim of the K-feldspar grains show an increase in orthoclase component (Figs. 4e and 6). In the same glimmerite sample, relict plagioclase (partially altered to Si-Al alteration product in fractures) have almost pure albite composition (Figs. 4e, 5a, b and 6).

To investigate the temperature of growth, titanium-in-biotite thermometry (Henry *et al.,* 2005) was performed on biotite in the main glimmerite schist (sample GD1606; Fig. 2e, f). Ti a.p.f.u. values are recorded in the range of 0.11–0.15 a.p.f.u with most of the values concentrated above 0.13 a.p.f.u (TiO_2 values of 2.03–2.63 wt%; Table S1). Biotite X_{Mg} values are recorded in the range of 0.53–0.58 a.p.f.u and mostly concentred up to 0.56 a.p.f.u (Fe: 16.25–17.82 wt%; Mg: 11.32–

12.55 wt%; Table S1) (Fig. S1). The calculated Ti concentration in biotite from glimmerite schist reflects an apparent temperature of growth of ~660 ± 50°C.

Coarse and interstitial K-feldspar grains from the glimmerite schist (sample GD1606; Fig. 4e and 5b; see also Fig. 10) have an overall enriched REE pattern compared to chondrite REE values (McDonough & Sun, 1995), with La > Lu and a progressive depletion pattern from La to Sm (Fig. 7a). From Gd to Lu, a faint concave-up shaped REE pattern is observed. Coarse K-feldspar grains have a slight increase in Eu in spot analyses located close to the rim of the grains (Fig. 7c). K-feldspar grains in the granitic lens (sample GD1620A) present a much higher variability in REE concentration between grains compared to those in the glimmerite schist (Fig. 7a). K-feldspar grains from both rock types display positive Eu anomalies except for one enriched grain within the granitic lens that shows a modest negative Eu pattern slope. Compiled data of K-feldspar REE values from rock types analogous to the samples analysed in this study show similarities to our analysed K-feldspars in granitic lens and glimmerite schist (Fig. 7a, b). The variability in REE patterns is most intense in the K-feldspar in granodiorite gneiss (Bingen *et al.,* 1990), followed by the K-feldspar-rich leucosome (Carvalho *et al.,* 2016) and lastly K-feldspar in pegmatite (Larsen, 2002).

4.4. Detailed microstructures and crystallographic orientation relationships

There are several mineralogically distinct bands at ~45° to the stretching lineation (Fig. 4a, 8). These are composed mainly of K-feldspar or quartz grains within an aggregate of K-feldspar, quartz and biotite of sigmoidal shape, specifically in between two C'-type planes forming a biotite shear band in thin section (Fig. 4a). The elongation of quartz grains is observed to follow the sigmoidal shapes of the mica fabric (in Fig. 8a black areas) and individual quartz grains apparently bend around K-feldspar grains, yet show little internal deformation (Fig. 8b). The quartz [c]-axis maximum presents a relatively weak and broad cluster (max. 2.6 mean angular deviation) parallel to the Z-axis and <a> axes are scattered along a pole figure primitive circle (Fig. 8c). Both J- and M-indices are low with 1.27 and 0.02, respectively. Pole figures for K-feldspar are presented in two

362 groups divided by grain size. The threshold for the division in coarse K-feldspar and interpreted
363 interstitial grains was set at 0.5% of the map area. The group of identified coarse K-feldspar grains
364 moderately clustered a-axes around the Z-axis and c-axes are clustered in the SW sector close to the
365 primitive circle, similar in orientation to the C'-type shear bands displayed in Fig. 8a. Interstitial K-
366 feldspar grains show some alignment with a J- and M-index of 2.44 and 0.03, respectively (Fig. 8c).
367 K-feldspar shows [c]-axis orientations dispersed 45° at the top and bottom on the X-axis pole figure.
368 The distribution of misorientation between pairs of quartz and K-feldspar shows nearly perfect
369 random distribution for quartz grains and weak correlation of misorientation distribution for K-
370 feldspar grains below 60° (Fig. 8c).

371 There are no internal changes to crystal orientation within the coarse K-feldspar grains,
372 nor are there any sub-grains present within the rims of the grains (Fig. 9). K-feldspar grains still
373 preserve relatively straight grains boundaries (crystal facets) when comparing the inferred boundaries
374 to a 3-dimensional representation of the grain orientation and crystallographic system (coloured
375 dashed lines; Fig. 9). Biotite and muscovite commonly protrude into the K-feldspar in the glimmerite
376 schist (Fig. 5a, c, e). These mica embayments are observed to preferentially follow the direction of
377 the crystal axes i.e., perpendicular to the crystal planes, of the K-feldspar grains (coloured arrows;
378 Fig. 9).

379 In the low-strain areas between the aligned K-feldspar grains, quartz grains exhibit
380 extensive formation of Dauphine twin boundaries (Fig. 10a), while the K-feldspar grains of all grain
381 sizes do not present any significant misorientation within individual grains (Fig. 10b). Similar to the
382 K-feldspar in Fig. 9, no sub-grain boundaries are observed. Two coarse interstitial quartz grains,
383 separated in 2-dimensions by the clustered small K-feldspar grains, present a misorientation between
384 them of less than 15° (Fig. 10a). Most of the clustered small K-feldspar grains exhibit similar
385 characteristics to the coarse K-feldspar grains (see Fig. 9) with limited crystal lattice bending,
386 relatively straight grain boundaries and biotite protrusions along the K-feldspar a, b and c axes (Fig.
387 10b). Two small K-feldspar grains that exhibit similar orientation are shown in Fig. 10b (pink grains).

Both these grains share grain boundaries with other small K-feldspar grains. The array of small K-feldspar grains in the strain shadow of the coarse K-feldspar grains share similar orientations (green colours on Fig. 10a inset), while the surrounding coarse K-feldspar grains also share a similar orientation to each other (pink colours on Fig. 10a inset), but different to the small interstitial grains.

5. DISCUSSION

Recent studies of the Alice Springs Orogeny and the Gough Dam shear zone show that high-strain zones are characterised by (1) prevalent microstructures indicative of the former presence of melt; (2) lack of plastic deformation and CPO in quartz; (3) an inferred correlation between increased time-integrated melt flux and increased temperature of biotite formation, along with increased REE and trace elements concentration, and (4) a complex monazite age pattern due to coupled dissolution-precipitation reactions mediated by interaction with melt (Piazolo *et al*., 2020; Silva *et al*., 2022). These studies further propose that the abundant glimmerite bands formed by hydration and addition of various elements, mostly K and Al, and in a lesser amount Na, Mg and Fe, during melt-rock interaction and the passage of melt through the GDSZ. The extent of melt-rock interaction forming glimmerite is controlled by the variability of (i) the composition of the melt source, (ii) extent of geochemical modification of the melt during reactive flow due to channel armouring, (iii) variation in rock types interacted along melt migration pathways, and (iv) possible trapping of early crystallised minerals (i.e., phenocrysts in the migrating melts) during the collapse of pathways as melt supply is reduced. Silva *et al*. (2022) calculated minimum time-integrated melt flux volumes of 0.03–0.23m^3 of melt per m^3 of rock, indicating large volumes of melt migrated through high-strain zones during the Alice Springs Orogeny. Recent work investigating the enrichment of oxide minerals in a high-strain zone immediately south of the GDSZ also inferred large volumes of melt are required to migrate through the high-strain zones in order to explain the observed enrichment (Ghatak, *et al*., 2022). Furthermore, the presence of melt during deformation in the GDSZ weakened the high-strain zone rheologically enhancing exhumation throughout the Alice Springs

414 Orogeny. While this study complements the previous research by examination and characterisation
415 of granitic lenses and other felsic components associated with hydration reactions forming
416 glimmerite, our focus here is to establish if the presence of coarse, faceted K-feldspar grains within
417 the glimmerite is a direct consequence of melt flux during deformation. If true, then such K-feldspar
418 grains represent a new indicator of the former presence of syntectonic and migrating melts.
419
420 **5.1 Syntectonic melt migration: From field to petrographic and microstructural evidence**
421 At the macro-scale, field relationships show both the biotite-rich and the biotite-poor
422 rocks have features typical of melt-present high-strain zones: (i) preferential mineral alignment
423 forming a distinct and well-developed foliation and lineation defined mainly by biotite and facetted
424 K-feldspar grains; (ii) lenses with granitic composition and coarse grains aligned along the foliation
425 resemble pinch and swell patterns; and (iii) elongated grains of quartz and feldspar in granitic
426 gneisses, with some K-feldspar grains exhibiting sigmoidal shapes (Fig. 2; Vernon, 1987; Lister &
427 Snoke, 1984; Passchier & Trouw, 2005). Although commonly formed during solid-state deformation,
428 the alignment of biotite or K-feldspar grains can also be produced by magmatic flow (Collins &
429 Sawyer, 1996; Paterson *et al.,* 1998; Vernon, 2000; Žák *et al.,* 2008; Zibra *et al.,* 2014). Close
430 examination of the granitic lenses shows that these present igneous characteristics including
431 interlocking, faceted feldspar grains of unimodal grain size, and interstitial quartz and plagioclase
432 (Figs. 2c, d and 3). Even though the trails of granitic lenses resemble pinch and swell structures, the
433 minerals constituting the lenses show little evidence for solid-state deformation (e.g., bimodal grains
434 size or mantled porphyroclast observed by, for example, Vernon *et al.* (1983) and Tullis & Yund
435 (1991)). There is a lack of evidence for solid-state deformation in the granitic lenses, such as dynamic
436 recrystallisation, (e.g., Kruse & Stünitz, 1999; Svahnberg & Piazolo, 2010) (Fig. 3b–e) which points
437 toward a differential stress regime synchronous with melt injection. The geometric shape and
438 arrangement of granitic lenses closely resemble the pseudo-boudinage of Bons *et al.* (2004) and
439 Druguet & Carreras (2006), in which they describe similar patterns resembling pinch and swell

structures in partially crystallised pegmatites. Importantly, the facetted nature of K-feldspar grains within granitic lenses (Fig. 3) is consistent with an igneous origin without significant post-crystallisation internal deformation or modification. This is a feature common to many high melt volume migmatites (Sawyer, 2008).

In the field, the schistose nature of the glimmerite (Fig. 2e–h) suggests grain alignment of all key minerals in the assemblage. This is supported by petrographic evidence for preferential grain alignment of biotite, K-feldspar, quartz, muscovite and sillimanite (Figs. 4 and 5). Differential stress is interpreted to cause preferential mineral alignment and polymineralic sigmoidal shaped structures comprising a combination of muscovite, K-feldspar and quartz (Fig. 4d; Passchier & Trouw, 2005), and biotite shear bands (C'-type; Berthé *et al.,* 1979) at ~45° to the foliation (Figs. 4a and 8a). However, close analysis of the minerals highlights very limited internal grain deformation and a distinct lack of features commonly observed in high-strain zones that deform in the solid-state (e.g., kinking and folding of biotite and/or undulose extinction in K-feldspar and quartz grains (Figs. 4a and 5e, f) (e.g., Wilson, 1980; Lister & Snoke, 1984). Development of mica fish, grain size reduction producing core-mantle structures and internal deformation structures such as subgrain boundaries and continuous crystal lattice bending, commonly attributed to solid-state crystal-plastic deformation (e.g., Ten Grotenhuis *et al.,* 2003; Passchier & Trouw, 2005; Mancktelow & Pennacchioni, 2005), are completely missing from the glimmerite schist (Figs. 4 and 5).

We suggest that the absence of a strain record in the individual grains comprising the glimmerite schist and granitic lenses is consistent with the presence of a weak intergranular medium, in this case, interstitial melt that accommodated a large part of the applied stresses via grain boundary sliding. This is similar to the experimental aggregate strength reduction with the increase of melt fraction in mylonites from Rosenberg & Handy (2005). Our model of melt-present deformation is supported by the following microstructures in the different samples described. At the edge of the granitic lenses, the described highly elongate grains of plagioclase and quartz (Fig. 3b, c) are interpreted as minerals that pseudomorphed grain boundary melt films (Holness & Sawyer, 2008). In

466 the glimmerite schist, melt–K-feldspar reaction can account for the presence of embayments
467 containing plagioclase, biotite and muscovite at the edge of coarse K-feldspar grains (Figs. 4e, 5a, c,
468 9 and 10b). These embayment reactions resemble a "back reaction" of the vapour absent melting
469 reaction: Ms + Qz + Pl = Kfs + Sil (or Ky) + Melt (Patiño Douce & Johnston, 1991). The quartz and
470 K-feldspar aggregates in the low-strain shadows between the coarse K-feldspar grains closely
471 resemble interstitial textures, consistent with melt-present deformation (Figs. 4a, d, e, 5b, c and 10).
472 The observation of weak CPO of quartz and K-feldspar, even though there is a strong foliation and
473 lineation, contradicts the common observation of high CPO intensity in solid-state crystal plastic
474 deformation at high strain (e.g., Lister & Hobbs, 1980; Law, 1990; Menegon *et al.,* 2008; Law *et al*.,
475 2010). However, this conundrum can be explained by the presence of melt during deformation which
476 accommodated most of the strain. In the low-pressure or strain shadow regions between coarse K-
477 feldspar grains, a trail of smaller K-feldspar grains resembling a deformation tail is observed (Figs.
478 4e, 5b and 10). This type of microstructure is commonly observed in deformed porphyroclasts present
479 in mylonite. However, in the latter scenario, the tails comprise recrystallised material from the
480 porphyroclast or the strain shadows comprise minerals formed by solid state crystal plasticity (i.e.,
481 dynamic recrystallisation) or dissolution-precipitation mechanisms, respectively (Yardley, 1977;
482 Vernon, 1987; Passchier & Trouw, 2005). Although resembling a deformation trail by dynamic
483 recrystallisation, the smaller K-feldspar trail does not present microstructures indicative of such a
484 process. This interpretation is informed by the lack of internal deformation and sub-grain formation
485 close to the coarse K-feldspar grain boundaries (Fig. 10) (Tullis & Yund, 1985; Ree *et al.,* 2005;
486 Menegon *et al.,* 2008, 2013). By contrast, some of the smaller isolated K-feldspar grains in the low-
487 pressure regions are connected in three dimensions, as they share the same crystallographic
488 orientation, indicating crystallisation from grain-boundary melt connected in 3D (Fig. 10b).
489 In addition, the microstructure of the embayments into the coarse K-feldspar grains is
490 unusual for a high-strain rock deformed by solid-state deformation (Passchier & Trouw, 2005; Figs.
491 9 and 10b). In the latter case, one would expect interlocking microstructure between these minerals.

Instead, a reactive nature of that contact, where K-feldspar is dissolved, and plagioclase-biotite-muscovite grow is more likely. The fact that this texture is undeformed but still aligned with the general foliation of the sample suggests formation at a time the rock was under differential stress. We suggest that this microstructure formed when melt-K-feldspar interaction triggered the dissolution of K-feldspar and precipitation of plagioclase-biotite-muscovite. This indicates that the melt involved in the reaction was different to that from which the K-feldspar grew, consistent with open system melt flux through the high-strain zone.

The low mode of quartz in the granitic lenses and in the glimmerite schist suggests that the silica-rich interstitial melt was physically removed from the system. Melt expulsion is caused by waning melt pressure relative to confining pressure and/or differential tectonic stress (Davidson *et al*., 1992, 1994; D'lemos *et al.*, 1992; Brown, 1994). In summary, the microstructures observed in the rocks of the GDSZ are consistent with high-strain melt-present deformation.

5.2. Origin of the coarse K-feldspar grains within glimmerite

The coarse K-feldspar grains observed as dominantly individual grains in the glimmerite schist are interpreted to have formed by early, ex-situ crystallisation of the interpreted migrating granite melt (Figs. 2e–g and 4). Other examples of concentration of K-feldspar are described in the literature (e.g., in granitoids [e.g., Vernon, 1986; Vernon & Paterson, 2008], in schlieren suggesting phenocryst flow-sorting [e.g., Bateman & Chappell, 1979; Vernon, 1986], and in enclaves in megacrystic granitoids [e.g., Didier, 1973]). The igneous origin of K-feldspar grains is further supported by the similarities between the K-feldspar grains of the granitic lenses which are of igneous origin, and the K-feldspar within the glimmerite. Similarities between K-feldspar grains in these two rocks include coarse grain size, conservation of faceted grains, low internal deformation and rare presence of small inclusions (Figs. 3–5).

The observed matrix foliation wrapping around the K-feldspar grains indicates pre- to syntectonic mineral growth, in our case in migrating granitic melt similar in composition to the

518 previously described granitic lenses (Figs. 4e and 5). Porphyroblasts in high-strain zones share this
519 characteristic and may also exhibit inclusion trails or sigmoidal shape commonly showing grain
520 rotation relative to the matrix foliation (Passchier *et al.,* 1992; Johnson, 1999). We use (1) the foliation
521 warping around the K-feldspar grains in addition to (2) preservation of crystal faces, (3) lack of
522 internal deformation and (4) lack of core-mantle microstructure, features indicating recrystallisation
523 by grain area reduction (Figs. 4e, 5, 9 and 10; see review of these microstructures in Passchier &
524 Trouw (2005) and Blenkinsop (2007)) to interpret the K-feldspar grains as early crystallising minerals
525 from the migrating melt. Following the described physical characteristics of the K-feldspar grains, an
526 alternative peritectic origin could be suggested for the formation of the K-feldspar phenocrysts (e.g.,
527 Sawyer, 2008; Cruciani *et al.*, 2008; Vernon, 2011; Dyck *et al.*, 2020). However, the peritectic
528 hypothesis is problematic when related to the following description of the K-feldspar microstructures
529 and reaction with entrapped melt. The shape of the K-feldspar has been weakly modified to form the
530 embayments by reaction replacement producing plagioclase, biotite and muscovite that we interpret
531 as due to grain–melt reaction subsequent to the K-feldspar grains being entrapped (Figs. 5a, 9 and
532 10b). The presence of entrapped melt is also observed in the granitic lenses in the form of elongated
533 interstitial plagioclase (Fig. 3c). It is apparent that reaction dissolution was enhanced along the
534 crystallographic b and c axes of the K-feldspar phenocrysts, similar in concept to the observed
535 forsterite anisotropic dissolution favouring crystallographic axes (Grandstaff, 1978; Awad *et al.,*
536 2000; Godinho *et al.,* 2013, 2014) or the preferential partial melting along subgrain boundaries in
537 quartz and plagioclase of Levine *et al.* (2016).

538 The K-feldspar grains exhibit no evident chemical zonation, except for some rim
539 domains showing a localised stronger positive Eu anomaly and a slight increase in orthoclase
540 component (Figs. 6 and 7c). This limited chemical zonation suggests that the crystallisation of the K-
541 feldspar grain in the migrating melt was fast, and that the crystallisation of melt was of short duration.
542 This model of K-feldspar crystallisation is informed by the tendency of feldspar grains to form
543 chemical zonation due to the strength of the Si-O and Al-O bonds (Winter, 2013) and/or by an open

system allowing the chemical or physical disruption of the boundary layer around the K-feldspar grain which is usually depleted in elements with mineral/melt partition coefficient > 1, allowing maximum crystal growth (Green & Watson, 1982; Bacon, 1989). The fast growth of the K-feldspar phenocrysts can be explained by reduced nucleation in highly hydrous silicate melts, as per the crystallisation mechanism of the igneous K-feldspar grains in the surrounding granitic lenses (Figs. 2a, c and 3). Once the mineral nucleates, fast mineral growth occurs at undercooled conditions (Nabelek *et al.,* 2010). The fast growth surrounded by melt allied to delayed nucleation possibly explains the rarity of small inclusions in K-feldspar grains and phenocrysts in both the glimmerite and granitic lenses (Figs. 3b–e, 5, 9 and 10). In experimental conditions, K-feldspar crystallisation begins with at least 60–70% of liquid in the crystal mush which may suggest that the phenocrysts grew in pockets of the fluxing melt with a high fraction of liquid (Clemens & Wall, 1981; Winkler & Schultes, 1982). The crystallisation of K-feldspar first is per the observed sequence of mineral crystallisation in granite, as extensively discussed by Vernon & Paterson (2008) for K-feldspar megacrysts in granite and zoned pegmatites that tend to form monomineralic segregations of K-feldspar or quartz, starting far from the liquidus with an initial assemblage of K-feldspar + quartz ± biotite (Cameron *et al.,* 1949; London, 2005). This may suggest that the melt migrating through the GDSZ may have had a chemical composition close to the aforementioned zoned pegmatites and the observed GDSZ granitic lenses due to the similarities in the observed sequence of mineral crystallisation (Fig. 3).

Some K-feldspar grains exhibit an increase in Eu and modal component of orthoclase at the rim of the grain (Figs. 6 and 7a, c). This increase in Eu concentration and orthoclase component occurs close to the embayments into the K-feldspar grains, suggesting that the contact with a subsequent melt triggers localised “back reaction”, discussed previously. This may locally modify the Eu concentration in the K-feldspar due to the high Kfs/melt Eu partition coefficient; the higher orthoclase component may be due to coupled exchange of Na and K at the reaction interface during formation of albite (Labotka *et al.,* 2004; Hövelmann *et al.,* 2010). The REE concentrations of the K-

570 feldspar in the granitic lenses show highly variable values between grains (Table 2 and Fig. 7a). This
571 variability contrasts with the mainly homogeneous REE pattern and enriched REE concentration of
572 K-feldspar in glimmerite schist (this study), magmatic K-feldspar in pegmatite and porphyroblastic
573 K-feldspar in granodiorite gneiss (Fig. 7b) (Larsen, 2002; Bingen *et al.,* 1990). However, the
574 variability in REE concentration values and overall patterns in the granitic lenses resembles the REE
575 patterns observed for migmatites in leucosome from Carvalho *et al.* (2016). This variability in REE
576 concentration values between grains can be explained by higher fractional crystallisation of K-
577 feldspar grains due to lower melt flow while mineral crystallisation occurred. The progressively
578 decreasing REE pattern of the K-feldspar from La to Lu in the glimmerite schist resembles the
579 patterns observed for some of the pegmatite K-feldspar and migmatite leucosome data (Fig. 7b). K-
580 feldspar grains in leucosome (Carvalho *et al.,* 2016) show depleted HREE compared to our K-feldspar
581 phenocrysts. This is explained by melt flow entrainment of accessory minerals with high HREE
582 affinity from the adjacent rock. The contrast in REE patterns suggests that this physical process is
583 unlikely to have taken place in the channelised melt flow forming the K-feldspar phenocrysts here.
584 The similarity in REE concentration pattern with pegmatites and migmatite leucosome is consistent
585 with a magmatic origin for the K-feldspar present in the glimmerite schist and our preserved
586 phenocryst interpretation.
587
588 **5.3. Trapped K-feldspar: A signature for melt fluxing and subsequent melt extraction and**
589 **associated physical collapse**
590 Following our interpretation of melt-present deformation in the GDSZ and supported
591 by similar conclusions by Piazolo *et al.* (2020) and Silva *et al.* (2022), and that the K-feldspar has an
592 igneous origin, one question remains: how did relatively undeformed K-feldspar grains end up in a
593 high-strain zone? We interpret a prolonged one-step process where the K-feldspar phenocrysts
594 crystallised in the channelised migrating melt and were trapped in the glimmerite schist during the
595 collapse of the melt pathways. We infer that a decrease in the melt supply (i.e., draining of the source),

implying a waning of the melt pressure, meant that the melt pressure could no longer maintain an open channel while confining pressure and tectonic stress were still significant, leading to the structural collapse of the system (e.g., Kisters *et al.*, 2009; Fig. 11).

In our model, we interpret the melt filling of tensional fractures along strike, possibly formed due to an anisotropic tensile strength of the protolith (Wickham, 1987), as the most probable mechanism for the initiation of the melt pathways observed in the study area. Additionally, the physical size of the K-feldspar grains also argues against a more pervasive grain boundary melt flow process that would have formed interconnected melt flow bands (Fig. 2a, c, d) (Brown, 1994; Weinberg, 1999; Bons *et al.,* 2004). Other indications of fracture propagation are observed in the orthogonal mode 1 extensional fractures in the quartzite mylonite layers surrounded by the glimmerite schist (Fig. 2h). The same development of pathways is believed to have happened early in the formation of the glimmerite schist. These pathways are not as visible in the glimmerite rock type due to the higher amount of melt-rock interaction producing glimmerite at the expense of adjacent rocks by dissolution-precipitation (Fig. 2b, h; Silva *et al.*, 2022). Furthermore, the grain shape and preferred orientation of the micas possibly facilitated the extraction of melt during the collapse of the high-strain zone (Figs. 4 and 5) (Weinberg *et al.,* 2001; Žák *et al.,* 2008). The presence of a melt fraction in the glimmerite schist during the period of deformation would have decreased the strength of the rock by several orders of magnitude and increased the temperature of biotite formation compared to the glimmerite bands adjacent to the modified granulite rocks (Fig. S1) (Rosenberg & Handy, 2005; Silva *et al.*, 2022). Extreme weakening increases non-linearly up to 10 vol% of melt fraction (melt connectivity transition of Rosenberg & Handy (2005)), with the melt lubricating 90% of crystal boundaries at the 10 vol% melt fraction threshold described by Van der Molen & Paterson (1979).

The final melt extraction and crystal entrapment occurred during the collapse of the high-strain zone when the combined confining pressure and tectonic stress finally overcame the melt pressure. The proposed formation of the trails of granitic lenses observed in the felsic bands (Fig. 2a, c, d) follow closely the model of Bons *et al*. (2004) and Druguet & Carreras (2006) for their

syntectonic melt deformation, inflation and collapse of pegmatite dykes in Cap de Creus, Spain. In Bons *et al.* (2004), one of the main features used to recognise collapse structures is the formation of thinning beads (Fig. 9a in Bons *et al.,* 2004) in partially crystallised pegmatite dykes. These can easily be interpreted as boudinage, in lieu of formation of collapse beads, due to the morphological similarities at outcrop scale (Bons *et al.,* 2004, 2008; Druguet & Carreras, 2006). During the process of collapse, most of the strain and foliation deflection is localised at the corner of the beads, decreasing away from these structures. These observations are at odds with the observed strain spanning the entire area in between boudins. Furthermore, no evidence of dyke-parallel stretching within the beads or in the thin seams connecting the beads are observed when pegmatite beads form by local inflation and collapse, usually observed in boudin formation (Bons *et al.,* 2004).

The overall main characteristics of the beads formation model of Bons *et al.* (2004, 2008) fit the observed lack of extensional deformation of the granitic lenses in our study area and the small amount of strain observed in between them (Figs. 2c, d and 3). Altogether, these structural characteristics of the granitic lenses fits the concept of pseudo-boudinage. The presence of a high vol% of melt during the period of deformation of the granitic lenses most probably allowed the strain to concentrate into the melt instead of the solid mineral grains (Vigneresse & Tikoff, 1999), resulting in little internal evidence of the synchronous high strain in the remaining beads. A similar process of melt filled fractures followed by collapse is proposed for the formation of the glimmerite schist. The sequence of melt inflation and later collapse would explain the presence and entrapment of K-feldspar phenocrysts in the glimmerite matrix and the entrapment and crystallisation of melt in low-strain regions of the glimmerite schist (Figs. 2e, f, 4e and 10). This collapse process would also explain the inferred melt extraction that mitigated the formation of granitic bodies within the glimmerite schist. This is also consistent with the small number of igneous microstructures observed in the glimmerite matrix and the lack of deformation of solid grains. Following the Bons *et al.* (2004) collapse model, we suggest that the contrast between the granitic lenses and the isolated K-feldspar crystals was due to differential concentration of crystals locally present during the collapse, leading to a decrease of

crystal entrapment with an increase of melt fraction.

6. CONCLUSIONS

The presence of undeformed and faceted K-feldspar phenocrysts as individual grains or clusters of grains in a high-strain zone of the Gough Dam shear zone, central Australia, occurred via the entrapment of entrained early crystallised minerals in channelised migrating melt due to the collapse of wall rocks constituting the melt pathway. The opening of melt pathways probably occurred by tensional fractures along rock anisotropies. This syndeformational creation of melt migration pathways in a high-strain zone allowed channelised melt flux, as observed by the presence of granitic lenses, and extensive melt-rock interaction. The melt-mediated reaction produced glimmerite schist and glimmerite, and involved dissolution of the adjacent felsic wall rocks. Early, fast-growing K-feldspar grains crystallised from the fluxing melt due to the delayed mineral nucleation in an undercooled and hydrous melt. The posterior collapse of the melt pathway, comprising glimmerite enriched walls, occurred following decreased melt supply. This ultimately led to the entrapment of the crystallised minerals (phenocrysts) in the melt and synchronous extraction of the remaining liquid fraction from the high-strain zone. This physical entrapment process allowed the formation of granitic lenses in less reacted melt pathways (granitic gneiss) and an increase in the efficiency of entrapment of phenocrysts in the more reacted glimmerite schist bands. We suggest the presence of undeformed K-feldspar in high-strain zones is a new indicator of the former passage of migrating melt through rock types with otherwise limited field evidence indicative of the former presence of melt during deformation.

ACKNOWLEDGMENTS

We thank the landowners for permission to access sample localities in the Gough Dam shear zone, central Australia. M. Bebbington, T. Murphy, Y-J. Lai and H. Ghatak (Macquarie University) assisted with making thin sections and geochemical analysis. Sandrin Feig (University of

674 Tasmania) assisted with electron microprobe analysis. Duncan Hedges and Richard Walshaw
675 (University of Leeds) assisted with EBSD data collection. This work was carried out as part of a PhD
676 study at Macquarie University and was supported by ARC Discovery grant DP160103449 to A.
677 Putnis, T. Raimondo and N. Daczko. We thank R. White (University of St. Andrews) and an
678 anonymous reviewer for constructive comments and editorial handling. We thank S. Cruden (Monash
679 University) and A. Tommasi (University of Montpellier) for feedback on an earlier version of this
680 manuscript. This study used instrumentation funded by ARC LIEF, DEST Systemic Infrastructure
681 Grants, NCRIS/AuScope, industry partners and Macquarie University. This is contribution 1745 from
682 the ARC Centre of Excellence for Core to Crust Fluid Systems (http://www.CCFS.mq.edu.au).
683

684 **SUPPLEMENTARY DATA**

685 Supplementary data are available at Journal of Metamorphic Geology online.

686

687 **REFERENCES**

688 Armstrong, J. T. (1988). Quantitative analysis of silicate and oxide materials: Comparison of Monte
689 Carlo, ZAF, and ψ (ρz) procedures. *Microbeam Analysis*, 239–246.

690 Awad A., van Groos A. F. K., & Guggenheim, S. (2000). Forsteritic olivine: effect of crystallographic
691 direction on dissolution kinetics. *Geochimica et Cosmochimica Acta, 64*(10), 1765–1772.

692 Bachmann, F., Hielscher, R., & Schaeben, H. (2010). Texture analysis with MTEX–free and open
693 source software toolbox. *Solid State Phenomena*, *160*, 63–68.

694 Bacon, C. R. (1989). Crystallization of accessory phases in magmas by local saturation adjacent to
695 phenocrysts. *Geochimica et Cosmochimica Acta*, *53*(5), 1055–1066.

696 Ballèvre, M., Hensen, B. J., & Reynard, B. (1997). Orthopyroxene-andalusite symplectites replacing
697 cordierite in granulites from the Strangways Range (Arunta block, central Australia): a new
698 twist to the pressure-temperature history. *Geology, 25*(3), 215–218.

699 Ballèvre, M., Möller, A., & Hensen, B. J. (2000). Exhumation of the lower crust during crustal
700 shortening: an Alice Springs (380 Ma) age for a prograde amphibolite facies shear zone in the
701 Strangways Metamorphic Complex (central Australia). *Journal of Metamorphic*
702 *Geology, 18*(6), 737–747.

703 Bateman, P. C. & Chappell, B, W. (1979). Crystallization, fractionation, and solidification of the
704 Tuolumne Intrusive Series, Yosemite National Park, California. *Bulletin of the Geological*
705 *Society of America, 90*(5), 465–482.

706 Bea, F., Pereira, M. D., & Stroh, A. (1994). Mineral/leucosome trace-element partitioning in a
707 peraluminous migmatite (a laser ablation-ICP-MS study). *Chemical Geology*, *117*(1–4), 291–
708 312.

709 Beere, W. (1975). A unifying theory of the stability of penetrating liquid phases and sintering
710 pores. *Acta Metallurgica*, *23*(1), 131–138.

711 Bendall, B. (2000). Mid-Palaeozoic shear zones in the Strangways Range: a record of intracratonic
712 tectonism in the Arunta Inlier, Central Australia (Doctoral dissertation). University of
713 Adelaide, Adelaide, Australia.

714 Berthé, D., Choukroune, P., & Jégouzo, P. (1979). Orthogneiss, mylonite and non coaxial
715 deformation of granites: the example of the South Armorican Shear Zone. *Journal of*
716 *Structural Geology*, *1*(1), 31–42.

717 Bingen, B., Demaiffe, D., & Hertogen, J. (1990). Evolution of feldspars at the amphibolite-granulite-
718 facies transition in augen gneisses (SW Norway): geochemistry and Sr
719 isotopes. *Contributions to Mineralogy and Petrology*, *105*(3), 275–288.

720 Blenkinsop, T. G. (2007). *Deformation Microstructures and Mechanisms in Minerals and Rocks*.
721 Springer Science & Business Media.

722 Bons, P. D. (1999). Apparent extensional structures due to volume loss. *Proceedings Estonian*
723 *Academy of Sciences, 48*, 3–14.

724 Bons, P. D., Becker, J. K., Elburg, M. A., & Urtson, K. (2009). Granite formation: stepwise
725 accumulation of melt or connected networks? *Earth and Environmental Science Transactions*
726 *of the Royal Society of Edinburgh*, *100*(1–2), 105–115.

727 Bons, P. D., Druguet, E., Castaño, L. M., & Elburg, M. A. (2008). Finding what is now not there
728 anymore: Recognizing missing fluid and magma volumes. *Geology*, *36*(11), 851–854.

729 Bons, P. D., Druguet, E., Hamann, I., Carreras, J., & Passchier, C. W. (2004). Apparent boudinage in
730 dykes. *Journal of Structural Geology*, *26*(4), 625–636.

731 Brown, M. (1994). The generation, segregation, ascent and emplacement of granite magma: the
732 migmatite-to-crustally-derived granite connection in thickened orogens. *Earth-Science*
733 *Reviews*, *36*(1–2), 83–130.

734 Brown, M. (2005). Synergistic effects of melting and deformation: an example from the Variscan
735 belt, western France. *Geological Society, London, Special Publications*, *243*(1), 205–226.

736 Brown, M. & Rushmer, T. (2006). *Evolution and Differentiation of the Continental Crust*. Cambridge
737 University Press.

738 Brown, M. & Solar, G. S. (1998). Shear-zone systems and melts: feedback relations and self-
739 organization in orogenic belts. *Journal of Structural Geology, 20*(2–3), 211–227.

740 Buick, I. S., Storkey, A., & Williams, I. S. (2008). Timing relationships between pegmatite
741 emplacement, metamorphism and deformation during the intra-plate Alice Springs Orogeny,
742 central Australia. *Journal of Metamorphic Geology*, *26*(9), 915–936.

743 Bunge, H. J. (2013). *Texture Analysis in Materials Science: Mathematical Methods*. Elsevier.

744 Cameron, E. N., Jahns, R. H., McNair, A. H., & Page, L. R. (1949). Internal structure of granitic
745 pegmatites. *Economic Geology Monograph*, *2*, 115 p.

746 Cartwright, I., Buick, I. S., Foster, D. A., & Lambert, D. D. (1999). Alice Springs age shear zones
747 from the southeastern Reynolds Range, central Australia. *Australian Journal of Earth*
748 *Sciences*, *46*(3), 355–363.

749 Carvalho, B. B., Sawyer, E. W., & Janasi, V. A. (2016). Crustal reworking in a shear zone:
750 transformation of metagranite to migmatite. *Journal of Metamorphic Geology*, *34*(3), 237–
751 264.

752 Clemens, J. D., & Wall, V. J. (1981). Origin and crystallization of some peraluminous (S-type)
753 granitic magmas. *The Canadian Mineralogist*, *19*(1), 111–131.

754 Collins, W. J., & Sawyer, E. W. (1996). Pervasive granitoid magma transfer through the lower–
755 middle crust during non-coaxial compressional deformation. *Journal of Metamorphic*
756 *Geology*, *14*(5), 565–579.

757 Collins, W., & Shaw, R. (1995). Geochronological constraints on orogenic events in the Arunta inlier:
758 a review. *Precambrian Research, 71*(1), 315–346.

759 Collins, W., & Teyssier, C. (1989). Crustal scale ductile fault systems in the Arunta inlier, central
760 Australia. *Tectonophysics, 158*(1), 49–66.

761 Cruciani, G., Franceschelli, M., Elter, F. M., Puxeddu, M., & Utzeri, D. (2008). Petrogenesis of Al–
762 silicate-bearing trondhjemitic migmatites from NE Sardinia, Italy. *Lithos*, *102*(3-4), 554–574.

763 D'lemos, R. S., Brown, M., & Strachan, R. A. (1992). Granite magma generation, ascent and
764 emplacement within a transpressional orogen. *Journal of the Geological Society*, *149*(4), 487–
765 490.

766 Daczko, N. R., & Piazolo, S. (2022). Recognition of melferite–A rock formed in syn-deformational
767 high-strain melt-transfer zones through sub-solidus rocks: A review and synthesis of
768 microstructural criteria. *Lithos*, 430–431, 106850.

769 Daczko, N. R., Piazolo, S., Meek, U., Stuart, C. A., & Elliott, V. (2016). Hornblendite delineates
770 zones of mass transfer through the lower crust. *Scientific Reports*, *6*(1), 1-6.

771 Davidson, C., Hollister, L. S., & Schmid, S. M. (1992). Role of melt in the formation of a deep-crustal
772 compressive shear zone: The MaClaren Glacier Metamorphic Belt, south central
773 Alaska. *Tectonics*, *11*(2), 348–359.

774 Davidson, C., Schmid, S. M., & Hollister, L. S. (1994). Role of melt during deformation in the deep
775 crust. *Terra Nova*, *6*(2), 133–142.

776 Didier, J. (1973). *Granites and their Enclaves: The Bearing of Enclaves on the Origin of Granites*.
777 Developments in Petrology, 3. Elsevier.

778 Diener, J. F., White, R. W., & Hudson, T. J. (2014). Melt production, redistribution and accumulation
779 in mid-crustal source rocks, with implications for crustal-scale melt transfer. *Lithos*, *200*,
780 212–225.

781 Druguet, E., & Carreras, J. (2006). Analogue modelling of syntectonic leucosomes in migmatitic
782 schists. *Journal of Structural Geology*, *28*(10), 1734–1747.

783 Dyck, B., Waters, D. J., St-Onge, M. R., & Searle, M. P. (2020). Muscovite dehydration melting:
784 Reaction mechanisms, microstructures, and implications for anatexis. *Journal of*
785 *Metamorphic Geology*, *38*(1), 29–52.

786 Etheridge, M. A., Daczko, N. R., Chapman, T., & Stuart, C. A. (2020). Mechanisms of melt extraction
787 during lower crustal partial melting. *Journal of Metamorphic Geology, 39*(1), 57–75.

788 Ghatak, H., Gardner, R. L., Daczko, N. R., Piazolo, S., & Milan, L. (2022). Oxide enrichment by
789 syntectonic melt-rock interaction. *Lithos*, *414*, 106617.

790 Godinho, J. R., Piazolo, S., & Evans, L. (2014). Simulation of surface dynamics during dissolution
791 as a function of the surface orientation: Implications for non-constant dissolution rates. *Earth*
792 *and Planetary Science Letters*, *408*, 163–170.

793 Godinho, J. R., Putnis, C. V., & Piazolo, S. (2013). Direct observations of the dissolution of fluorite
794 surfaces with different orientations. *Crystal Growth & Design*, *14*(1), 69–77.

795 Grandstaff, D. E. (1978). Changes in surface area and morphology and the mechanism of forsterite
796 dissolution. *Geochimica et Cosmochimica Acta*, *42*(12), 1899–1901.

797 Green, T. H., & Watson, E. B. (1982). Crystallization of apatite in natural magmas under high
798 pressure, hydrous conditions, with particular reference to 'orogenic' rock
799 series. *Contributions to Mineralogy and Petrology*, *79*(1), 96–105.

800 Griffin, W. L. (2008). GLITTER: data reduction software for laser ablation ICP-MS. *Laser Ablation*
801 *ICP-MS in the Earth Sciences: Current practices and outstanding issues*, 308–311.

802 Haines, P. W., Hand, M., & Sandiford, M. (2001). Palaeozoic synorogenic sedimentation in central
803 and northern Australia: a review of distribution and timing with implications for the evolution
804 of intracontinental orogens. *Australian Journal of Earth Sciences*, *48*(6), 911–928.

805 Hand, M., & Sandiford, M. (1999). Intraplate deformation in central Australia, the link between
806 subsidence and fault reactivation. *Tectonophysics, 305*(1), 121–140.

807 Heinrich, K. F. J. (1966). X-ray absorption uncertainty. *The electron microprobe*, 296.

808 Henke, B. L. (1985). Lawrence Berkeley Laboratories, unpublished.

809 Henry, D. J., Guidotti, C. V., & Thomson, J. A. (2005). The Ti-saturation surface for low-to-medium
810 pressure metapelitic biotites: Implications for geothermometry and Ti-substitution
811 mechanisms. *American Mineralogist*, *90*(2-3), 316–328.

812 Henry, H. (2018) Mantle Pyroxenites: Deformation and Seismic Properties. (Doctoral dissertation).
813 Macquarie University, Sydney, Australia.

814 Henry, H., Tilhac, R., Griffin, W. L., O'Reilly, S. Y., Satsukawa, T., Kaczmarek, M. A., & Ceuleneer,
815 G. (2017). Deformation of mantle pyroxenites provides clues to geodynamic processes in
816 subduction zones: case study of the Cabo Ortegal Complex, Spain. *Earth and Planetary*
817 *Science Letters*, *472*, 174–185.

818 Hollister, L. S. & Crawford, M. L. (1986). Melt-enhanced deformation: a major tectonic process.
819 *Geology, 14*(7), 558–561.

820 Holness, M. B., & Sawyer, E. W. (2008). On the pseudomorphing of melt-filled pores during the
821 crystallization of migmatites. *Journal of Petrology*, *49*(7), 1343–1363.

822 Hövelmann, J., Putnis, A., Geisler, T., Schmidt, B. C., & Golla-Schindler, U. (2010). The replacement
823 of plagioclase feldspars by albite: observations from hydrothermal
824 experiments. *Contributions to Mineralogy and Petrology*, *159*(1), 43–59.

825 Hutton, D. H. (1988). Granite emplacement mechanisms and tectonic controls: Inferences from
826 deformation studies. *Earth and Environmental Science Transactions of the Royal Society of*
827 *Edinburgh*, *79*(2–3), 245–255.

828 Jarosewich, E., Nelen, J. A., & Norberg, J. A. (1980). Reference samples for electron microprobe
829 analysis. *Geostandards Newsletter, 4*(1), 43–47.

830 Johnson, S. E. (1999). Porphyroblast microstructures: a review of current and future trends. *American*
831 *Mineralogist*, *84*(11–12), 1711–1726.

832 Kisters, A. F. M., Ward, R. A., Anthonissen, C. J., & Vietze, M. E. (2009). Melt segregation and far-
833 field melt transfer in the mid-crust. *Journal of the Geological Society*, *166*(5), 905–918.

834 Kriegsman, L. M. (2001). Partial melting, partial melt extraction and partial back reaction in anatectic
835 migmatites. *Lithos*, *56*(1), 75–96.

836 Kruse, R., & Stünitz, H. (1999). Deformation mechanisms and phase distribution in mafic high-
837 temperature mylonites from the Jotun Nappe, southern Norway. *Tectonophysics*, *303*(1-4),

223–249.

Labotka, T. C., Cole, D. R., Fayek, M., Riciputi, L. R., & Stadermann, F. J. (2004). Coupled cation and oxygen-isotope exchange between alkali feldspar and aqueous chloride solution. *American Mineralogist*, *89*(11–12), 1822–1825.

Larsen, R. B. (2002). The distribution of rare-earth elements in K-feldspar as an indicator of petrogenetic processes in granitic pegmatites: Examples from two pegmatite fields in southern Norway. *The Canadian Mineralogist*, *40*(1), 137–152.

Law, R. D. (1990). Crystallographic fabrics: a selective review of their applications to research in structural geology. *Geological Society, London, Special Publications*, *54*(1), 335–352.

Law, R. D., Mainprice, D., Casey, M., Lloyd, G. E., Knipe, R. J., Cook, B., & Thigpen, J. R. (2010). Moine thrust zone mylonites at the Stack of Glencoul: I–microstructures, strain and influence of recrystallization on quartz crystal fabric development. *Geological Society, London, Special Publications*, *335*(1), 543–577.

Lee, A. L., Torvela, T., Lloyd, G. E., & Walker, A. M. (2018). Melt organisation and strain partitioning in the lower crust. *Journal of Structural Geology*, *113*, 188–199.

Levine, J. S. F., Mosher, S., & Siddoway, C. S. (2013). Relationship between syndeformational partial melting and crustal-scale magmatism and tectonism across the Wet Mountains, central Colorado. *Lithosphere, 5*(5), 456–476.

Levine, J. S., Mosher, S., & Rahl, J. M. (2016). The role of subgrain boundaries in partial melting. *Journal of Structural Geology*, *89*, 181–196.

Lister, G. S., & Hobbs, B. E. (1980). The simulation of fabric development during plastic deformation and its application to quartzite: the influence of deformation history. *Journal of Structural Geology*, *2*(3), 355–370.

Lister, G. S., & Snoke, A. W. (1984). S-C mylonites. *Journal of Structural Geology*, *6*(6), 617–638.

862 London, D. (2005). Granitic pegmatites: an assessment of current concepts and directions for the
863 future. *Lithos*, *80*(1–4), 281–303.

864 Maidment, D., Hand, M., & Williams, I. (2005). Tectonic cycles in the Strangways Metamorphic
865 Complex, Arunta inlier, central Australia: Geochronological evidence for exhumation and
866 basin formation between two high-grade metamorphic events. *Australian Journal of Earth*
867 *Sciences, 52*(2), 205–215.

868 Mancktelow, N. S., & Pennacchioni, G. (2005). The control of precursor brittle fracture and fluid–
869 rock interaction on the development of single and paired ductile shear zones. *Journal of*
870 *Structural Geology*, *27*(4), 645–661.

871 Marchildon, N., & Brown, M. (2003). Spatial distribution of melt-bearing structures in anatectic rocks
872 from southern Brittany, France: implications for melt transfer at grain-to orogen-
873 scale. *Tectonophysics*, *364*(3–4), 215–235.

874 Mawby, J., Hand, M., & Foden, J. (1999). Sm-Nd evidence for high–grade ordovician metamorphism
875 in the Arunta block, central Australia. *Journal of Metamorphic Geology, 17*(6), 653–668.

876 McDonough, W. F., & Sun, S. S. (1995). The composition of the Earth. *Chemical Geology*, *120*(3–
877 4), 223–253.

878 Meek, U., Piazolo, S., & Daczko, N. R. (2019). The field and microstructural signatures of
879 deformation-assisted melt transfer: Insights from magmatic arc lower crust, New
880 Zealand. *Journal of Metamorphic Geology*, *37*(6), 795–821.

881 Menegon, L., Pennacchioni, G., Heilbronner, R., & Pittarello, L. (2008). Evolution of quartz
882 microstructure and c-axis crystallographic preferred orientation within ductilely deformed
883 granitoids (Arolla unit, Western Alps). *Journal of Structural Geology*, *30*(11), 1332–1347.

884 Menegon, L., Stünitz, H., Nasipuri, P., Heilbronner, R., & Svahnberg, H. (2013). Transition from
885 fracturing to viscous flow in granulite facies perthitic feldspar (Lofoten, Norway). *Journal of*
886 *Structural Geology*, *48*, 95–112.

887 Nabelek, P. I., Whittington, A. G., & Sirbescu, M. L. C. (2010). The role of H2O in rapid
888 emplacement and crystallization of granite pegmatites: Resolving the paradox of large crystals
889 in highly undercooled melts. *Contributions to Mineralogy and Petrology*, *160*(3), 313–325.

890 Passchier, C. W., & Trouw, R. A. (2005). *Microtectonics*. Springer Science & Business Media.

891 Passchier, C. W., Trouw, R. A. J., Zwart, H. J., & Vissers, R. L. M. (1992). Porphyroblast rotation:
892 eppur si muove*?. *Journal of Metamorphic Geology*, *10*(3), 283–294.

893 Paterson, S. R., Fowler Jr., T. K., Schmidt, K. L., Yoshinobu, A. S., Yuan, E. S., & Miller, R. B.
894 (1998). Interpreting magmatic fabric patterns in plutons. *Lithos 44*(1–2), 53–82.

895 Patiño Douce, A. E., & Johnston, A. D. (1991). Phase equilibria and melt productivity in the pelitic
896 system: implications for the origin of peraluminous granitoids and aluminous
897 granulites. *Contributions to Mineralogy and Petrology*, *107*(2), 202–218.

898 Piazolo, S., Daczko, N., Silva, D., & Raimondo, T. (2020). Melt-present shear zones enable
899 intracontinental orogenesis. *Geology 48*(7), 643–648.

900 Raimondo, T., Clark, C., Hand, M., & Faure, K. (2011). Assessing the geochemical and tectonic
901 impacts of fluid-rock interaction in mid-crustal shear zones: a case study from the
902 intracontinental Alice Springs orogen, central Australia. *Journal of Metamorphic Geology,*
903 *29*(8), 821–850.

904 Raimondo, T., Hand, M., & Collins, W. J. (2014). Compressional intracontinental orogens: Ancient
905 and modern perspectives. *Earth–Science Reviews, 130*, 128–153.

906 Rasband, W. S. (1997–2018). ImageJ, U. S. National Institutes of Health. Bethesda, MD, USA.
907 Available at: http://imagej.nih.gov/ij/.

908 Ree, J. H., Kim, H. S., Han, R., & Jung, H. (2005). Grain-size reduction of feldspars by fracturing
909 and neocrystallization in a low-grade granitic mylonite and its rheological
910 effect. *Tectonophysics*, *407*(3–4), 227–237.

911 Rosenberg, C. L., & Handy, M. R. (2005). Experimental deformation of partially melted granite
912 revisited: implications for the continental crust. *Journal of Metamorphic Geology*, *23*(1), 19–
913 28.

914 Sawyer, E. W. (2008). *Atlas of migmatites* (Vol. 9). NRC Research press.

915 Scrimgeour, I. R. (2013). Developing a revised framework for the Arunta Region. In: Munson, T. J.,
916 Scrimgeour, I. R. (eds.), Annual Geoscience Exploration Seminar (AGES) Record of
917 Abstracts. Northern Territory Geological Survey, Record 2003-001, Darwin, 1–8.

918 Searle, M. (2013). Crustal melting, ductile flow, and deformation in mountain belts: cause and effect
919 relationships. *Lithosphere 5*(6), 547–554.

920 Shaw, R. D., Stewart, A. T., & Black, L. P. (1984). The Arunta Inlier: a complex ensialic mobile belt
921 in central Australia. Part 2: tectonic history. *Australian Journal of Earth Sciences*, *31*(4), 457–
922 484.

923 Silva, D., Daczko, N., Piazolo, S., Raimondo, T. (2022). Glimmerite: a product of melt-rock
924 interaction within a crustal-scale high-strain zone. *Gondwana Research, 105*, 160–184.

925 Silva, D., Piazolo, S., Daczko, N. R., Houseman, G., Raimondo, T., & Evans, L. (2018).
926 Intracontinental orogeny enhanced by far-field extension and local weak
927 crust. *Tectonics*, *37*(12), 4421–4443.

928 Skemer, P., Katayama, I., Jiang, Z., & Karato, S. I. (2005). The misorientation index: Development
929 of a new method for calculating the strength of lattice-preferred
930 orientation. *Tectonophysics*, *411*(1–4), 157–167.

931 Stuart, C. A., Daczko, N. R., & Piazolo, S. (2017). Local partial melting of the lower crust triggered
932 by hydration through melt–rock interaction: an example from Fiordland, New Zealand.
933 *Journal of Metamorphic Geology, 35*(2), 213–230.

934 Stuart, C. A., Piazolo, S., & Daczko, N. R. (2018). The recognition of former melt flux through high-

strain zones. *Journal of Metamorphic Geology*, *36*(8), 1049–1069.

Svahnberg, H., & Piazolo, S. (2010). The initiation of strain localisation in plagioclase-rich rocks: Insights from detailed microstructural analyses. *Journal of Structural Geology*, *32*(10), 1404–1416.

Ten Grotenhuis, S. M., Trouw, R. A. J., & Passchier, C. W. (2003). Evolution of mica fish in mylonitic rocks. *Tectonophysics*, *372*(1–2), 1–21.

Tetley, M. G., & Daczko, N. R. (2014). Virtual Petrographic Microscope: a multi-platform education and research software tool to analyse rock thin-sections. *Australian Journal of Earth Sciences*, *61*(4), 631–637.

Teyssier, C. (1985). A crustal thrust system in an intracratonic tectonic environment. *Journal of Structural Geology, 7*(6), 689–700.

Tullis, J., & Yund, R. A. (1985). Dynamic recrystallization of feldspar: a mechanism for ductile shear zone formation. *Geology*, *13*(4), 238–241.

Tullis, J., & Yund, R. A. (1991). Diffusion creep in feldspar aggregates: experimental evidence. *Journal of Structural Geology*, *13*(9), 987–1000.

Van der Molen, I., & Paterson, M. S. (1979). Experimental deformation of partially-melted granite. *Contributions to Mineralogy and Petrology*, *70*(3), 299–318.

Varga, J., Raimondo, T., Hand, M., Curtis, S., & Daczko, N. (2022). Hydration, melt production and rheological weakening within an intracontinental gneiss dome. *Lithos*, 432–433, 106872.

Vernon, R. H. (1986). K-feldspar megacrysts in granites—phenocrysts, not porphyroblasts. *Earth-Science Reviews*, *23*(1), 1–63.

Vernon, R. H. (1987). Growth and concentration of fibrous sillimanite related to heterogeneous deformation in K-feldspar-sillimanite metapelites. *Journal of Metamorphic Geology*, *5*(1), 51–68.

959 Vernon, R. H. (2000). Review of microstructural evidence of magmatic and solid-state flow. *Visual*
960 *Geosciences*, *5*(2), 1–23.

961 Vernon, R. H. (2011). Microstructures of melt-bearing regional metamorphic rocks. *Geological*
962 *Society of America Memoirs*, *207*, 1–11.

963 Vernon, R. H., & Paterson, S. R. (2008). How late are K-feldspar megacrysts in
964 granites? *Lithos*, *104*(1–4), 327–336.

965 Vernon, R. H., Williams, V. A., & D'arcy, W. F. (1983). Grain-size reduction and foliation
966 development in a deformed granitoid batholith. *Tectonophysics*, *92*(1–3), 123–145.

967 Vigneresse, J. L. (1995). Crustal regime of deformation and ascent of granitic magma.
968 *Tectonophysics, 249*(3–4), 187–202.

969 Vigneresse, J. L., & Tikoff, B. (1999). Strain partitioning during partial melting and crystallizing
970 felsic magmas. *Tectonophysics*, *312*(2–4), 117–132.

971 Von Bargen, N., & Waff, H. S. (1986). Permeabilities, interfacial areas and curvatures of partially
972 molten systems: results of numerical computations of equilibrium microstructures. *Journal of*
973 *Geophysical Research: Solid Earth*, *91*(B9), 9261–9276.

974 Weinberg, R. F. (1999). Mesoscale pervasive felsic magma migration: alternatives to dyking. *Lithos*
975 *46*(3), 393–410.

976 Weinberg, R. F., Hasalová, P., Ward, L., & Fanning, C. M. (2013). Interaction between deformation
977 and magma extraction in migmatites: Examples from Kangaroo Island. *South Australia*
978 *Bulletin, 125*(7–8), 1282–1300.

979 Weinberg, R. F., Sial, A. N., & Mariano, G. (2004). Close spatial relationship between plutons and
980 shear zones. *Geology*, *32*(5), 377–380.

981 Weinberg, R. F., Sial, A. N., & Pessoa, R. R., (2001). Magma flow within the Tavares pluton,
982 northeastern Brazil: Compositional and thermal convection. *Geological Society of America*
983 *Bulletin*, *113*(4), 508–520.

984 Whitney, D. L., & Evans, B. W. (2010). Abbreviations for names of rock-forming minerals. *American*
985 *Mineralogist*, *95*(1), 185–187.

986 Wickham, S. M. (1987). The segregation and emplacement of granitic magmas. *Journal of the*
987 *Geological Society*, *144*(2), 281–297.

988 Wilson, C. J. L. (1980). Shear zones in a pegmatite: a study of albite-mica-quartz
989 deformation. *Journal of Structural Geology*, *2*(1–2), 203–209.

990 Winkler, H. G. F., & Schultes, H. (1982). On the problem of alkali feldspar phenocrysts in granitic-
991 rocks. *Neues Jahrbuch fur Mineralogie Monatshefte*, *12*, 558–564.

992 Winter, J. D. (2013). *Principles of Igneous and Metamorphic Petrology*. Pearson education, London,
993 UK.

994 Wolfram, L. C., Weinberg, R. F., Hasalová, P., & Becchio, R. (2017). How melt segregation affects
995 granite chemistry: Migmatites from the Sierra de Quilmes, NW Argentina. *Journal of*
996 *Petrology*, *58*(12), 2339–2364.

997 Yardley, B. W. (1977). The nature and significance of the mechanism of sillimanite growth in the
998 Connemara Schists, Ireland. *Contributions to Mineralogy and Petrology*, *65*(1), 53–58.

999 Žák, J., Verner, K., & Týcová, P. (2008). Grain-scale processes in actively deforming magma mushes:
1000 New insights from electron backscatter diffraction (EBSD) analysis of biotite schlieren in the
1001 Jizera granite, Bohemian Massif. *Lithos*, *106*(3–4), 309–322.

1002 Závada, P., Schulmann, K., Konopásek, J., Ulrich, S., & Lexa, O. (2007). Extreme ductility of
1003 feldspar aggregates—Melt-enhanced grain boundary sliding and creep failure: Rheological

implications for felsic lower crust. *Journal of Geophysical Research: Solid Earth*, *112*(B10210), 1–15.

Zibra, I., Gessner, K., Smithies, H. R., & Peternell, M. (2014). On shearing, magmatism and regional deformation in Neoarchean granite-greenstone systems: Insights from the Yilgarn Craton. *Journal of Structural Geology*, *67*(B), 253–267.

FIGURE CAPTIONS

Fig. 1. Geological map of the SE Arunta Region showing study and sample locality (red star). The map emphasises the distribution of regional high-strain zones of hydrous schistose composition (e.g., Gough Dam shear zone, #1; yellow structures and respective number in map) in the mostly granulite and amphibolite facies rocks incorporating the Arunta Region. Represented are the regional anastomosing high-strain zones and thrust faults relative to the Strangways Metamorphic Complex (SMC) and the Harts Range Group (HRG). Simplified structural cross-sections (modified after Raimondo *et al.,* 2014) display the principal crustal discontinuities and high-strain zones of the main geological domains in the Arunta Region associated with the Alice Springs Orogeny (Collins & Teyssier, 1989; Ballèvre *et al.,* 2000; Maidment *et al.*, 2005; Raimondo *et al.,* 2011; Scrimgeour, 2013). #1 Gough Dam shear zone (GDSZ); #2 West Bore shear zone; #3 Wallaby Knob shear zone; #4 Yambah shear zone; #5 Southern Cross shear zone; #6 Harry Creek shear zone (HCSZ); #7 Erontonga/Two Mile Bore shear zone; #8 Illogwa shear zone; #9 Delny shear zone.

Fig. 2. Field relationships of the Gough Dam shear zone including sample localities. (a) Outcrop presenting biotite-rich glimmerite schist bands (white arrows) and trails of granitic lenses along the foliation (red arrows), both cutting a host of modified felsic granulite and granitic gneiss (S1: N102°/70°); (b) Outcrop of meter-scale glimmerite schist with a well-developed foliation (S1) that contains layers and lenses of partially modified relict felsic rock types. Field sense of shear is top to

1029 the north (S1: N78°/70°); (c, d) Outcrop-scale and detailed views of domains of the GDSZ containing
1030 a high abundance of variably deformed granitic lenses and glimmerite bands cutting modified granitic
1031 gneiss along foliation. Granitic lenses present asymmetric envelopes or selvedges of glimmerite
1032 composition; (e, f) Magnification of glimmerite schist outcrop containing granitic lenses, along with
1033 isolated and clustered facetted K-feldspar grains aligned along the foliation in the biotite dominated
1034 matrix of the glimmerite schist; (g) Hand sample and detailed view of the collected glimmerite schist
1035 used for petrographic study containing isolated and clustered, facetted, mm- to cm-wide K-feldspar
1036 grains; (h) Quartzite mylonite layer hosted by glimmerite schist. Glimmerite shows a reaction
1037 replacement relationship that "invades" the quartzite mylonite fractures in multiple directions.

1038

1039 **Fig. 3.** Hand specimen and petrographic characteristics of granitic lenses. (a) Hand samples
1040 GD1620A (left) and GD1617 (right) of granitic lens in modified granitic gneiss without and with
1041 glimmerite selvedge, respectively. Coloured dashed lines shows contact of granitic lens with granitic
1042 gneiss; (b) Crossed-polarised photomicrograph of granitic lens and its contact with granitic gneiss in
1043 sample GD1620A. Evidence of elongated interstitial plagioclase in (c) and low dihedral angles in (d)
1044 (see Fig. 2a for field relationship); (e) Crossed-polarised photomicrograph of extremity of granitic
1045 lens bead in modified granitic gneiss featuring a glimmerite selvedge (sample GD1617). Quartz grain
1046 from modified granitic gneiss in glimmerite selvedge shows embayments filled with biotite and
1047 interstitial quartz, occasionally with low apparent dihedral angles between two biotite grains (see Fig.
1048 2c, d for field relationship).

1049

1050 **Fig. 4.** Petrographic characteristics of glimmerite schist, sample GD1606. (a) Crossed-polarised light
1051 thin-section photomicrograph of glimmerite schist sample showing top to the left (reverse) shear-
1052 sense informed by sigmoidal shapes formed by biotite, muscovite, quartz and sillimanite grains
1053 around subangular K-feldspar and muscovite grains. Biotite-rich C'-type shear bands are observed.
1054 Photomicrographs for region (b) and (c) display dominant biotite glimmerite matrix showing

preferred orientation following C'-type shear band and S-plane, respectively; (d) Thin section μ-XRF mineral assemblage map; (e) SEM-BSE image of agglomeration of K-feldspar grains along the foliation. Dashed lines highlight biotite, muscovite, quartz and sillimanite grains warping around subangular K-feldspar grains. Embayments of biotite and muscovite in K-feldspar are highlighted by yellow arrows.

Fig. 5. Detailed microstructural characteristics of glimmerite schist, SEM-BSE and crossed-polarised light photomicrographs; sample GD1606. (a–d) Glimmerite schist sample presenting reaction replacement of (1) K-feldspar by biotite, muscovite and plagioclase "invasions" in embayments [panel a–c]; (2) low-pressure area between the trail of coarse K-feldspar grains presenting wrapping biotite band and interstitial quartz and trail of small K-feldspar grains [panel b]; and (3) coarse muscovite grain featuring a pressure shadow tail comprising biotite, quartz and minor K-feldspar grains [panel d]; (e, f) Crossed-polarised light photomicrographs of the featured region in panel (b) and (c) displaying the orientation and microstructures of the dominant biotite, quartz and muscovite present in the bands that warp around K-feldspar and located along the S-plane. Mineral abbreviations follow Whitney & Evans (2010).

Fig. 6. Mineral chemistry of K-feldspar core, rim and interstitial grains plotted on An-Ab-Or ternary diagram classification.

Fig. 7. K-feldspar grains chondrite-normalised REE patterns. (a) REE patterns for a diverse set of K-feldspar (isolated coarse grains and interstitial grains) in glimmerite schist and K-feldspar coarse grains in a granitic lens; (b) REE patterns plot from literature of non-GDSZ located K-feldspar present in pegmatite (Larsen, 2002), K-feldspar from leucocratic segregation in migmatites (Bea *et al.,* 1994; Carvalho *et al.,* 2016) and K-feldspar from the matrix of a granodiorite gneiss at granulite facies

(Bingen *et al.,* 1990); (c) REE patterns from K-feldspar rims (red lines) and interstitial grains (green lines; see Fig. 4e) possibly enriched in Eu compared to K-feldspar cores (black lines).

Fig. 8. Quantitative orientation analysis of K-feldspar and quartz; sample GD1606. (a) EBSD mineral phase map for quartz (red) and K-feldspar grains (blue) in glimmerite schist. Polymineralic sigmoidal shape and C'-type shear bands are indicated by the dashed white lines; (b) IPF-derived map for quartz grains relative to the X-plane; (c) Pole figures for all quartz grains and two groups of K-feldspar divided by grain size area, with a threshold at 0.5 per cent of map area, to distinguish coarse grains from interstitial grains. J- and M-index are displayed for all quartz grains and for interstitial K-feldspar grains. Uncorrelated misorientation angles distribution is featured for all grains from each mineral.

Fig. 9. Crystallographic misorientation map and embayments orientation of coarse K-feldspar grain. EBSD map comprised of band contrast and textural components showing the change in orientation within one coarse grain colour coded by crystallographic orientation divergence up to 5° relative to a reference orientation point. Coloured arrows highlight dissolution reaction sites on the K-feldspar grain and replacement by non-indexed minerals, i.e., mainly biotite and muscovite (top plane-polarised light photomicrograph), forming along the crystallographic axes of the K-feldspar grain. Quartz grains represented by variably grey EBSD band contrast, with rare sub-grain boundaries in yellow and common Dauphine twins in red. K-feldspar orientations of crystal faces are marked as coloured dashed lines.

Fig. 10. EBSD Euler and crystallographic misorientation maps of quartz and K-feldspar grains in glimmerite schist. (a) Interstitial low-strain area between two coarse K-feldspar grains presenting isolated quartz grains at a maximum misorientation of 15° relative to a reference point. Inset displays

1105 Euler colours of K-feldspar grains showing two main orientation groups (pink versus green colours).
1106 Quartz grains are coloured red. Euler angle rotation is coloured as ψ - red, θ - green and φ – blue; (b)
1107 K-feldspar grain analysis for misorientation from a reference point up to 15° with each colour
1108 representing a different grain analysis. Embayments and their orientation are highlighted by the
1109 direction of the coloured arrows that match the coloured lines highlighting the orientation of relict K-
1110 feldspar grain facets shown in the pole figures for a, b and c crystallographic planes (equal area, lower
1111 hemisphere projection). The orientations of crystal faces are transferred to the EBSD map image as
1112 coloured dashed lines.

1113

1114 **Fig. 11.** Cartoon illustrating the proposed model of melt transfer zone collapse and subsequent
1115 entrapment of crystallised fraction from the externally derived migrating melt.

1116

1117 **Table 1:** Selected electron microprobe data on multiple minerals for glimmerite schist present in
1118 GDSZ.

1119

1120 **Table 2:** Representative REE composition of K-feldspar grains from GDSZ and non-GDSZ
1121 published data from multiple locations.

1122

1123 **SUPPLEMENTARY MATERIAL**

1124 **Fig. S1.** Biotite in glimmerite schist Ti a.p.f.u. vs X_{Mg} a.p.f.u. graphical plot and Ti-in-biotite
1125 thermometry value estimation.

1126

1127 **Table S1:** Electron microprobe data of K-feldspar, plagioclase and biotite from glimmerite schist in
1128 the Gough Dam shear zone.

1129

1130 **Table S2:** LA-ICP-MS K-feldspar trace element data.

1131

Fig. 1

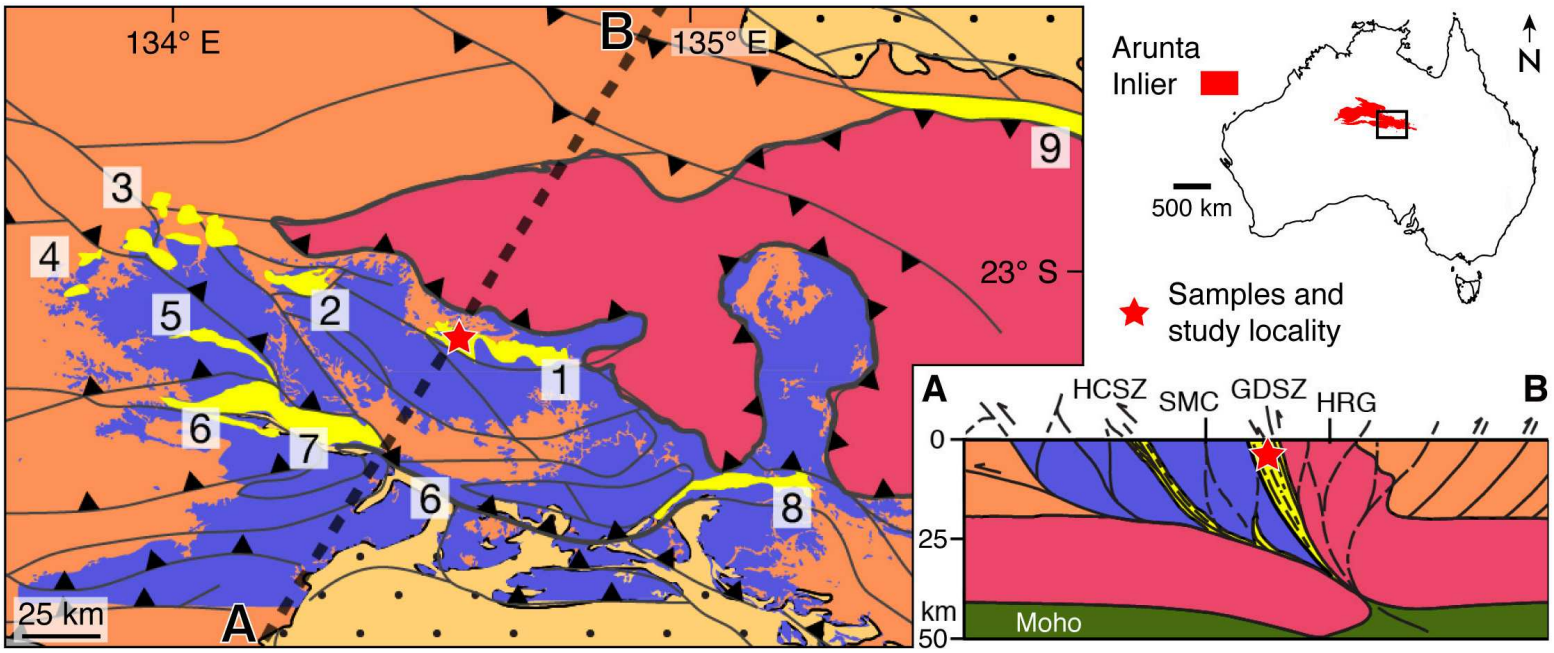

Schistose high strain zones

Strangways Metamorphic Complex (SMC)

Amphibolite facies rocks

Granulite facies rocks

Proterozoic-Palaeozoic intracontinental basins

Anastomosing shear zones

Fig. 2

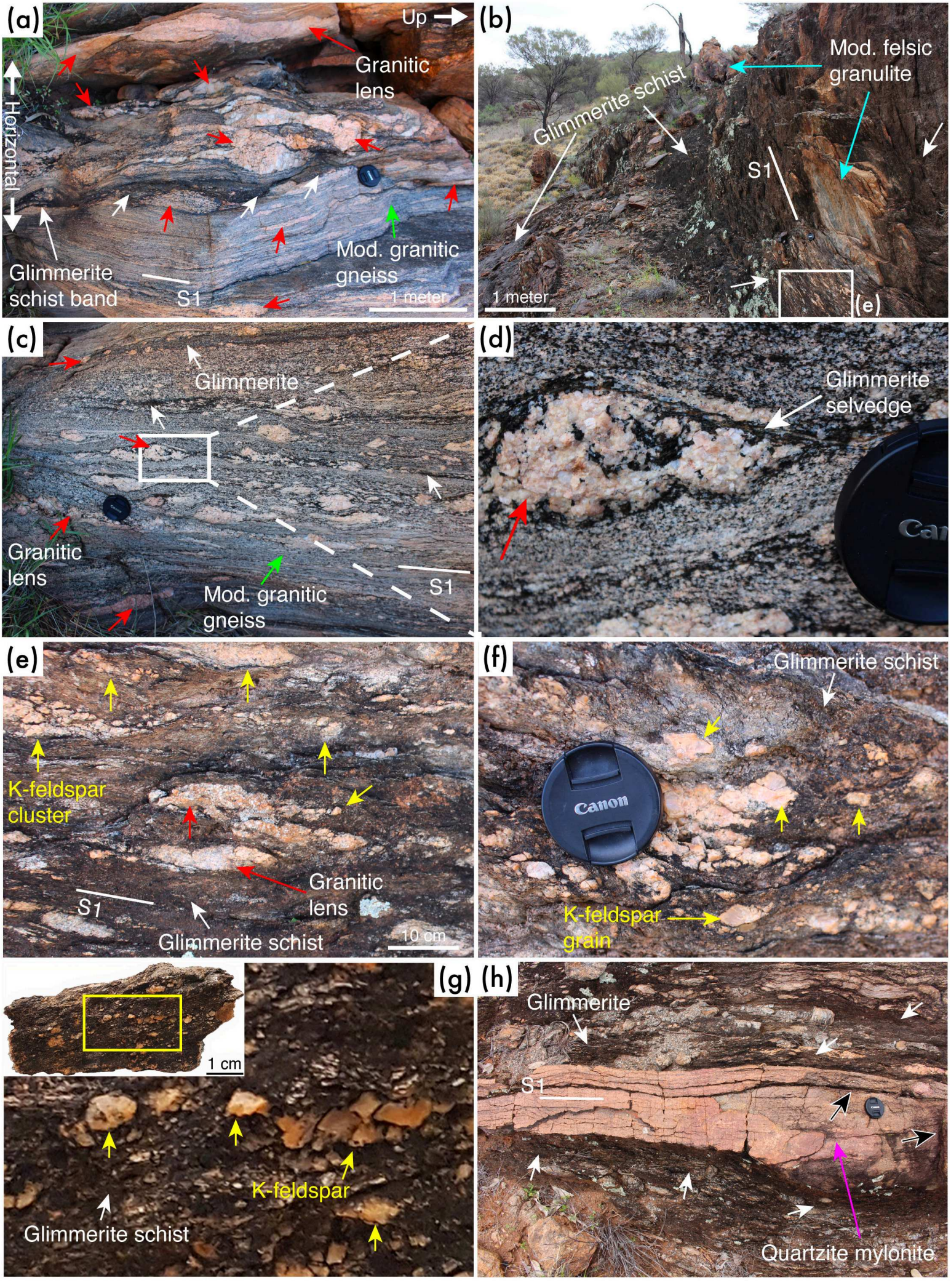
(a)
Up
Granitic lens
Horizontal
Glimmerite schist band
S1
Mod. granitic gneiss
1 meter
(b)
Mod. felsic granulite
Glimmerite schist
S1
1 meter
(e)
(c)
Glimmerite
Granitic lens
Mod. granitic gneiss
S1
(d)
Glimmerite selvedge
(e)
K-feldspar cluster
Granitic lens
S1
Glimmerite schist
10 cm
(f)
Glimmerite schist
Canon
K-feldspar grain
(g)
1 cm
K-feldspar
Glimmerite schist
(h)
Glimmerite
S1
Quartzite mylonite

Fig. 3

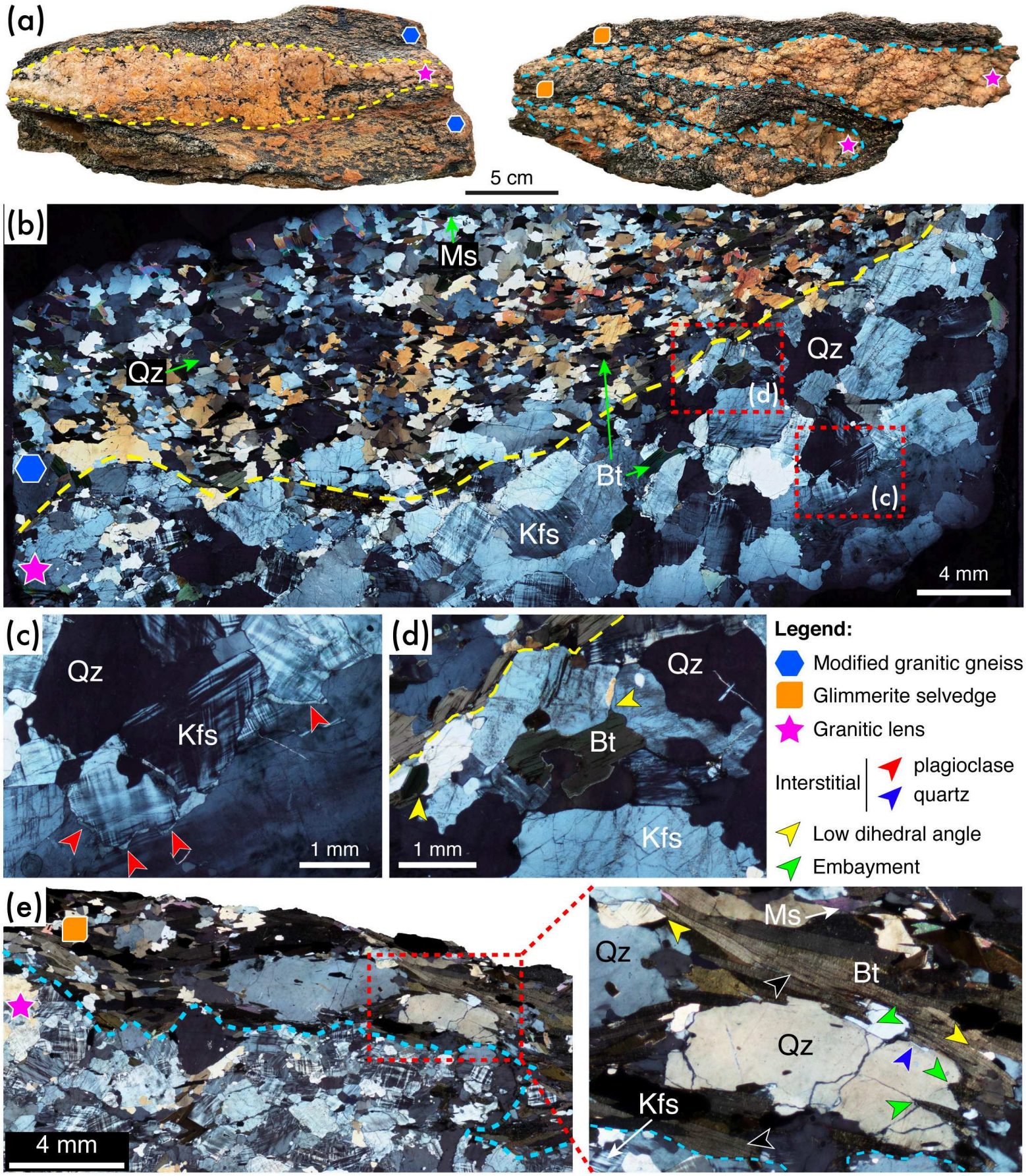
(a)
5 cm
(b)
Ms
Qz
Qz
(d)
Bt
(c)
Kfs
4 mm
(c)
Qz
Kfs
1 mm
(d)
Qz
Bt
Kfs
1 mm
Legend:
Modified granitic gneiss
Glimmerite selvedge
Granitic lens
Interstitial
plagioclase
quartz
Low dihedral angle
Embayment
(e)
4 mm
Ms
Qz
Bt
Qz
Kfs

Fig. 4

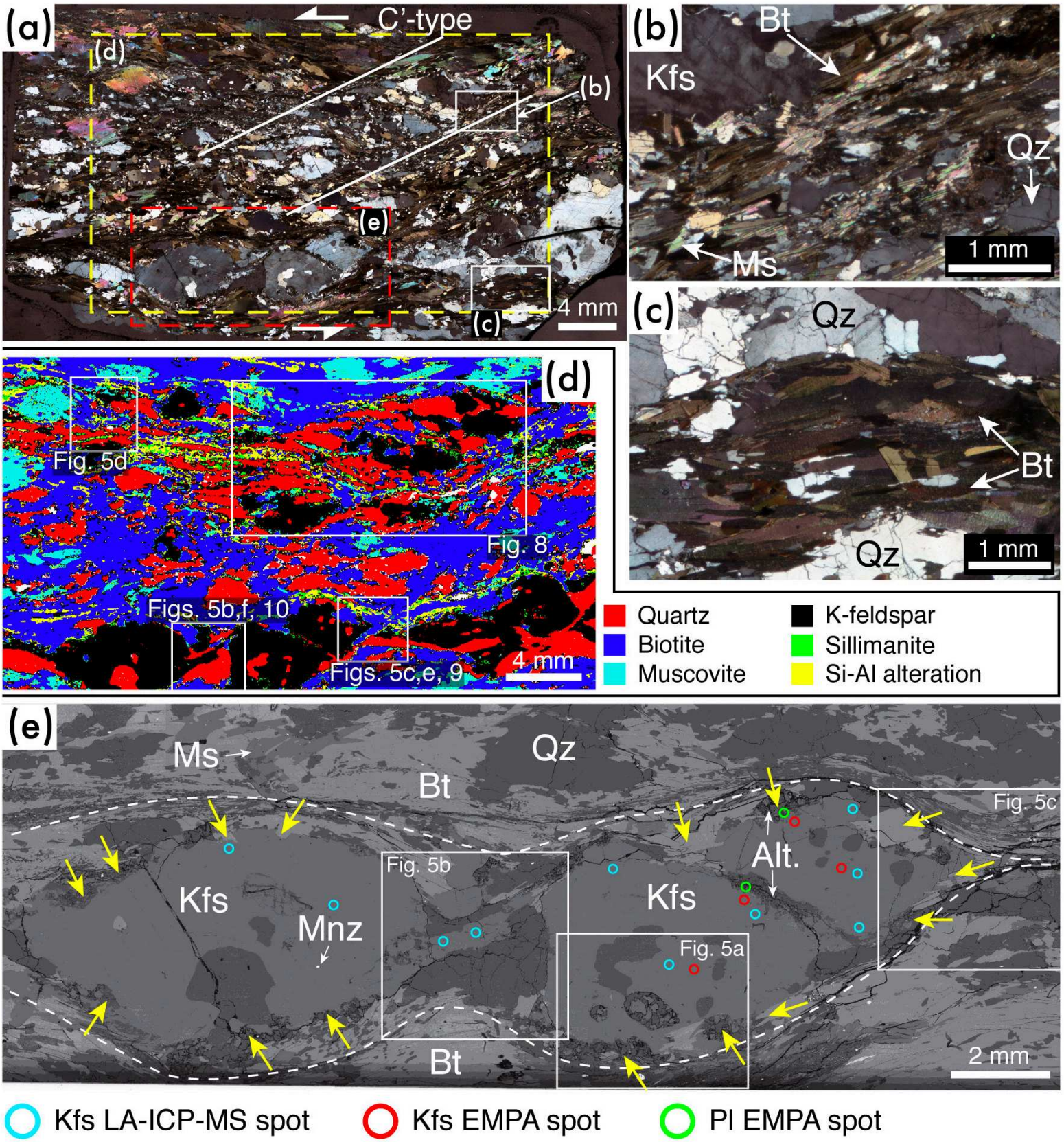
(a)
C'-type
(d)
(b)
(e)
(c)
4 mm
(b)
Bt
Kfs
Qz
Ms
1 mm
(c)
Qz
Bt
Qz
1 mm
(d)
Fig. 5d
Fig. 8
Figs. 5b,f, 10
Figs. 5c,e, 9
4 mm
Quartz
Biotite
Muscovite
K-feldspar
Sillimanite
Si-Al alteration
(e)
Ms
Qz
Bt
Fig. 5c
Alt.
Fig. 5b
Kfs
Kfs
Mnz
Fig. 5a
Bt
2 mm
Kfs LA-ICP-MS spot
Kfs EMPA spot
Pl EMPA spot

Fig. 5

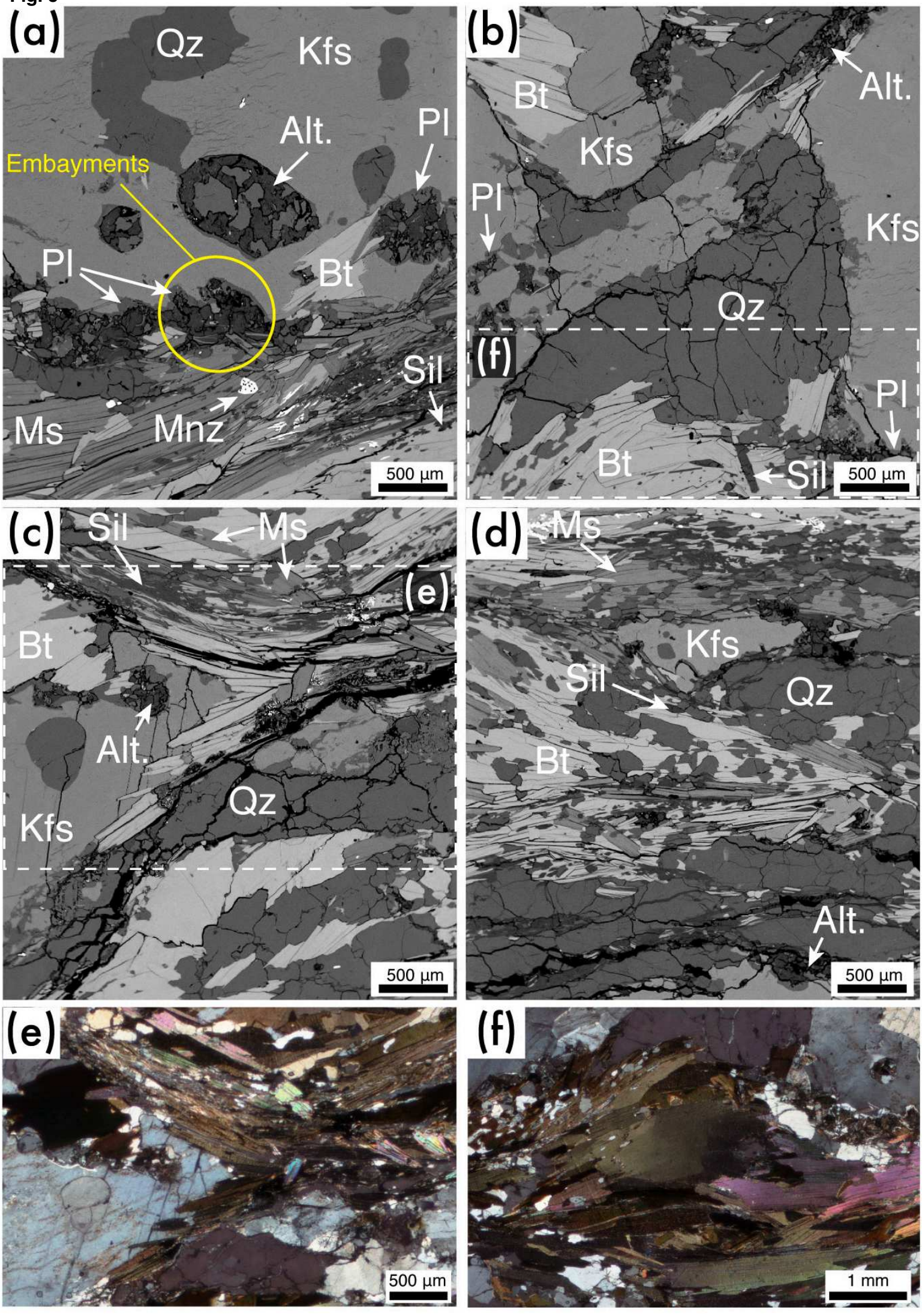
(a)
Qz
Kfs
Alt.
Pl
Embayments
Pl
Bt
Sil
Ms
Mnz
500 µm
(b)
Alt.
Bt
Kfs
Pl
Kfs
Qz
(f)
Pl
Bt
Sil
500 µm
(c)
Sil
Ms
(e)
Bt
Alt.
Qz
Kfs
500 µm
(d)
Ms
Kfs
Sil
Qz
Bt
Alt.
500 µm
(e)
500 µm
(f)
1 mm

Fig. 6

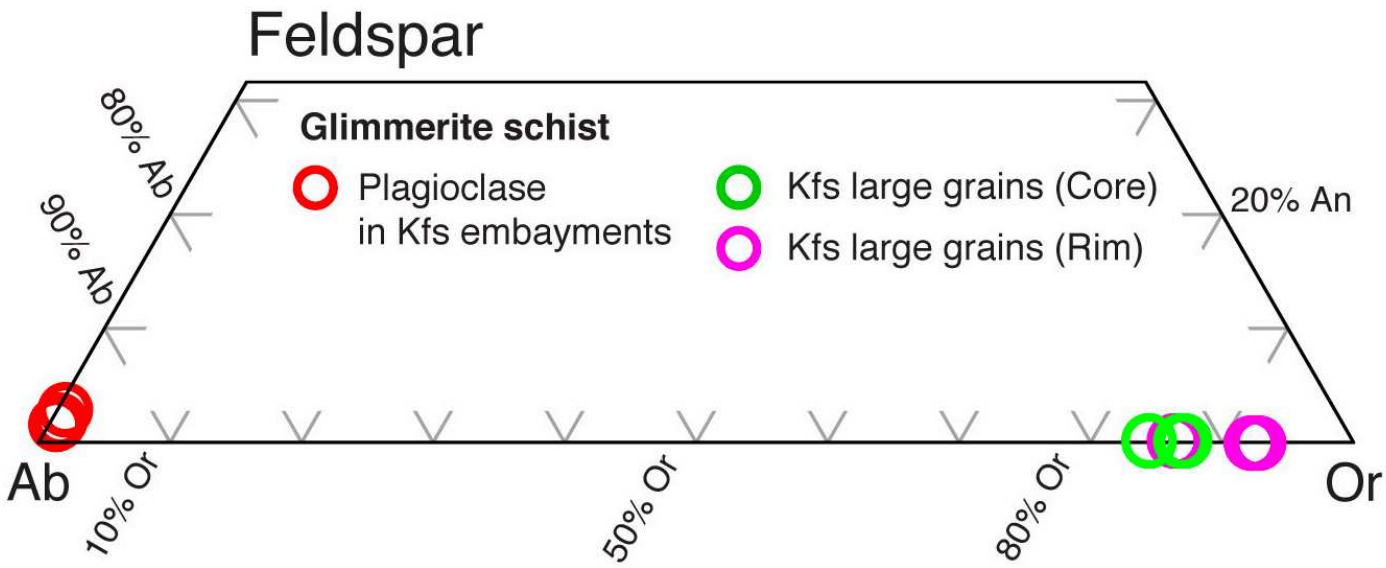
Feldspar
Glimmerite schist
Plagioclase
in Kfs embayments
Kfs large grains (Core)
Kfs large grains (Rim)
80% Ab
90% Ab
20% An
Ab
10% Or
50% Or
80% Or
Or

Fig. 7

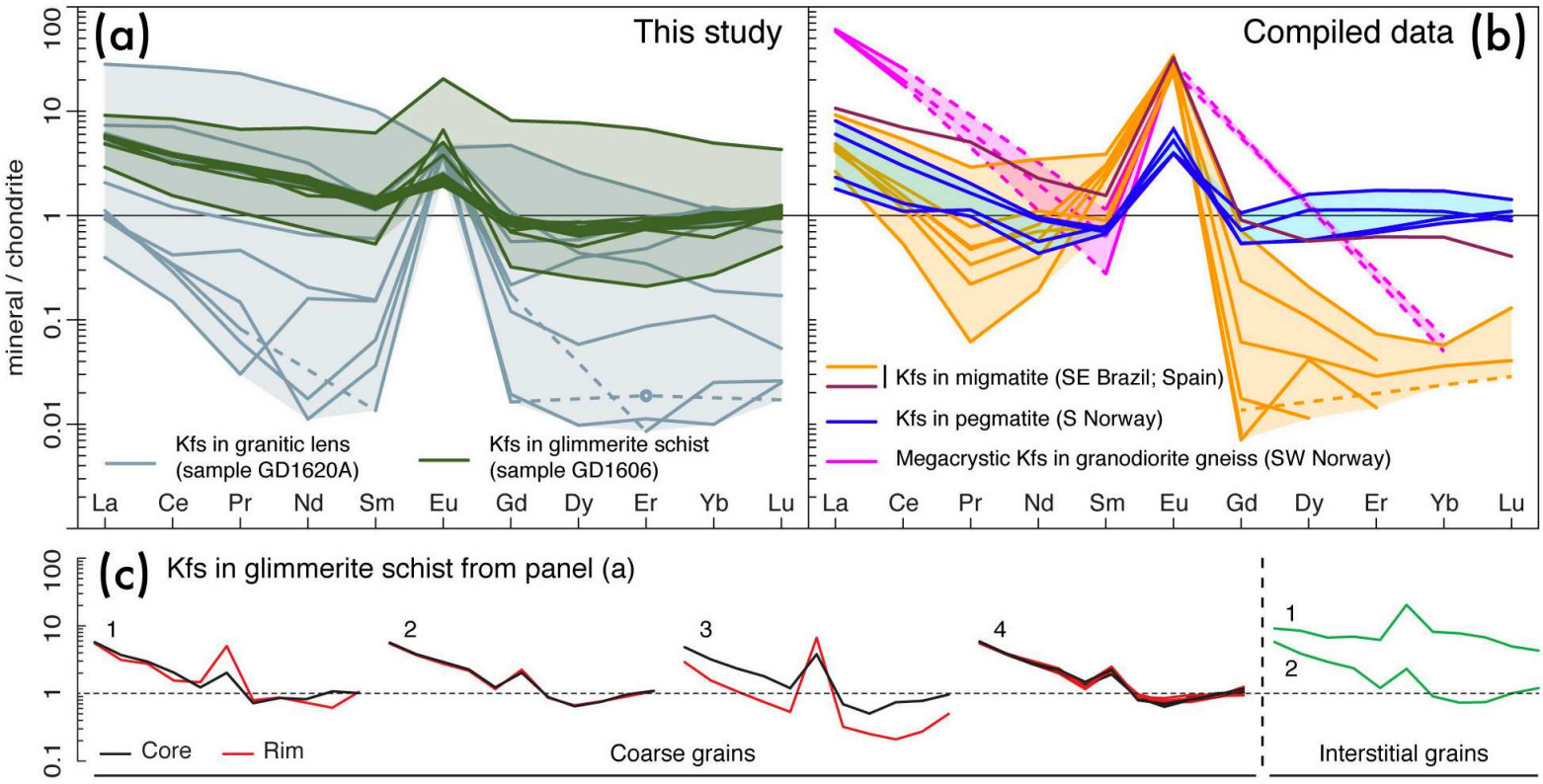
(a)
This study
(b)
Compiled data
mineral / chondrite
100
10
1
0.1
0.01
La Ce Pr Nd Sm Eu Gd Dy Er Yb Lu
Kfs in granitic lens (sample GD1620A)
Kfs in glimmerite schist (sample GD1606)
Kfs in migmatite (SE Brazil; Spain)
Kfs in pegmatite (S Norway)
Megacrystic Kfs in granodiorite gneiss (SW Norway)
(c)
Kfs in glimmerite schist from panel (a)
1
2
3
4
Core
Rim
Coarse grains
Interstitial grains

Fig. 8

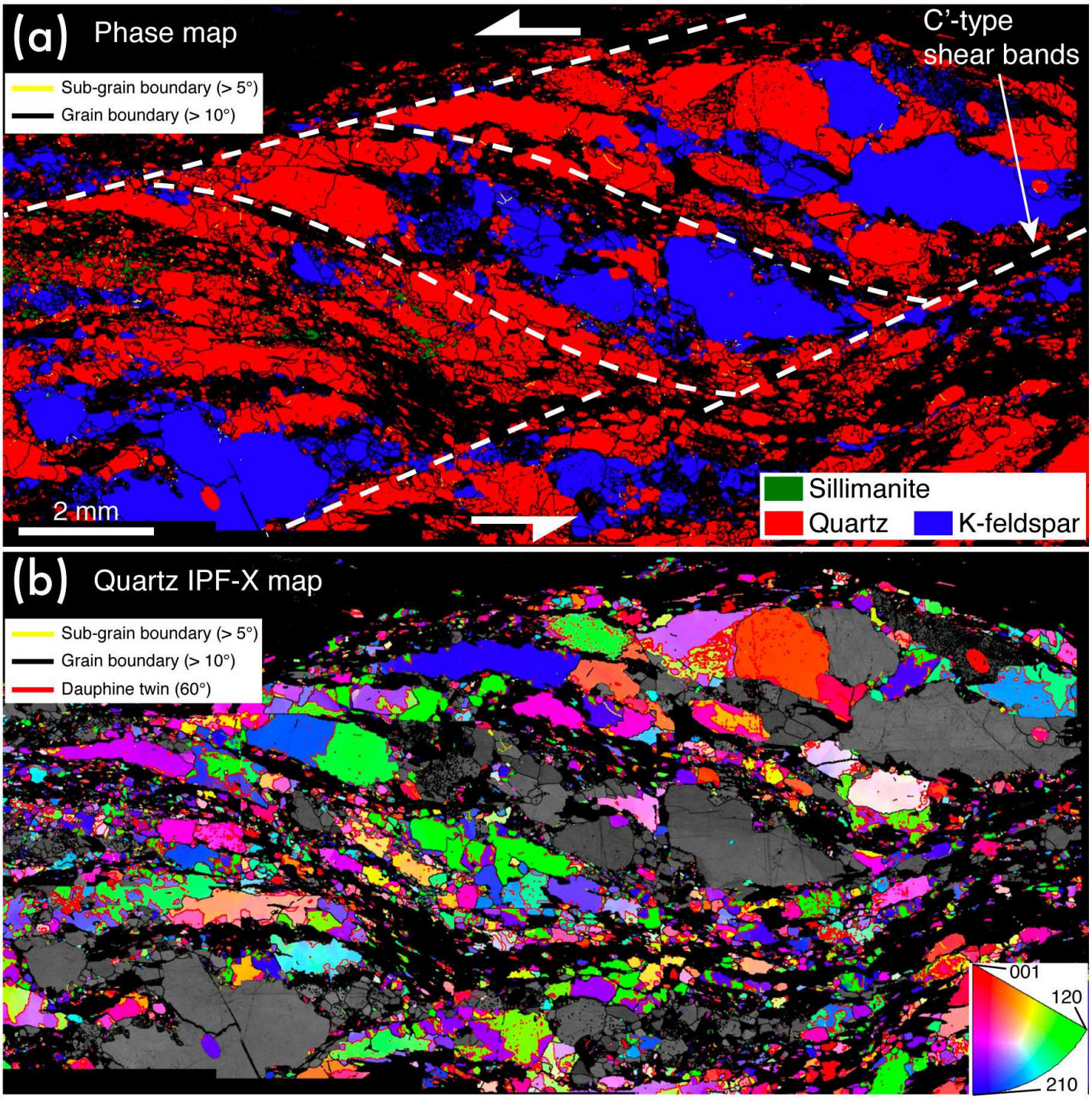
(a) Phase map
Sub-grain boundary (> 5°)
Grain boundary (> 10°)
C'-type shear bands
2 mm
Sillimanite
Quartz
K-feldspar

(b) Quartz IPF-X map
Sub-grain boundary (> 5°)
Grain boundary (> 10°)
Dauphine twin (60°)
001
120
210

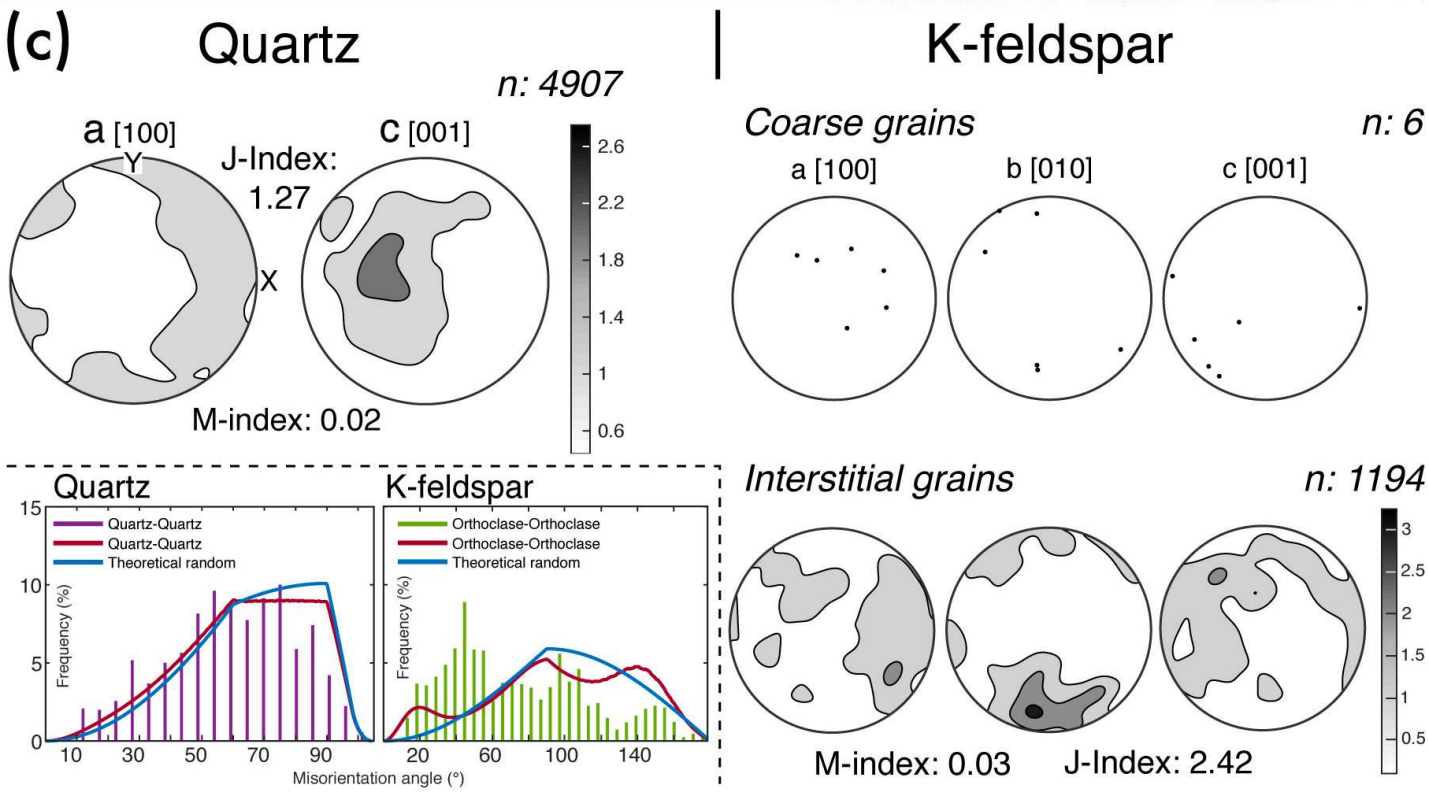
(c)
Quartz
n: 4907
a [100]
c [001]
Y
X
J-Index: 1.27
M-index: 0.02
2.6
2.2
1.8
1.4
1
0.6
K-feldspar
Coarse grains
n: 6
a [100]
b [010]
c [001]
Quartz
K-feldspar
Quartz-Quartz
Quartz-Quartz
Theoretical random
Orthoclase-Orthoclase
Orthoclase-Orthoclase
Theoretical random
Frequency (%)
Misorientation angle (°)
Interstitial grains
n: 1194
M-index: 0.03
J-Index: 2.42
3
2.5
2
1.5
1
0.5

Fig. 9

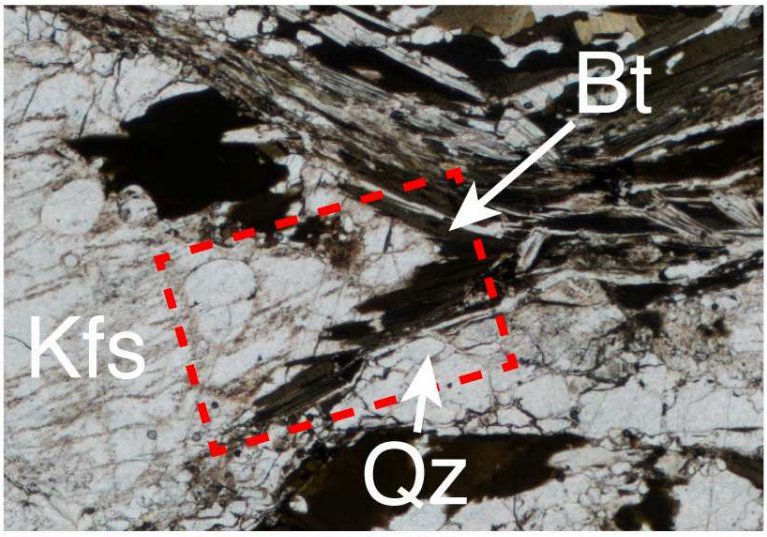

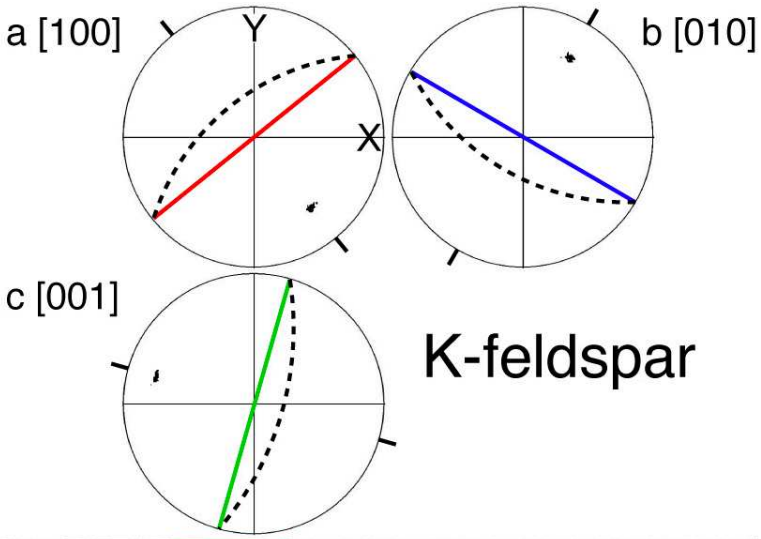

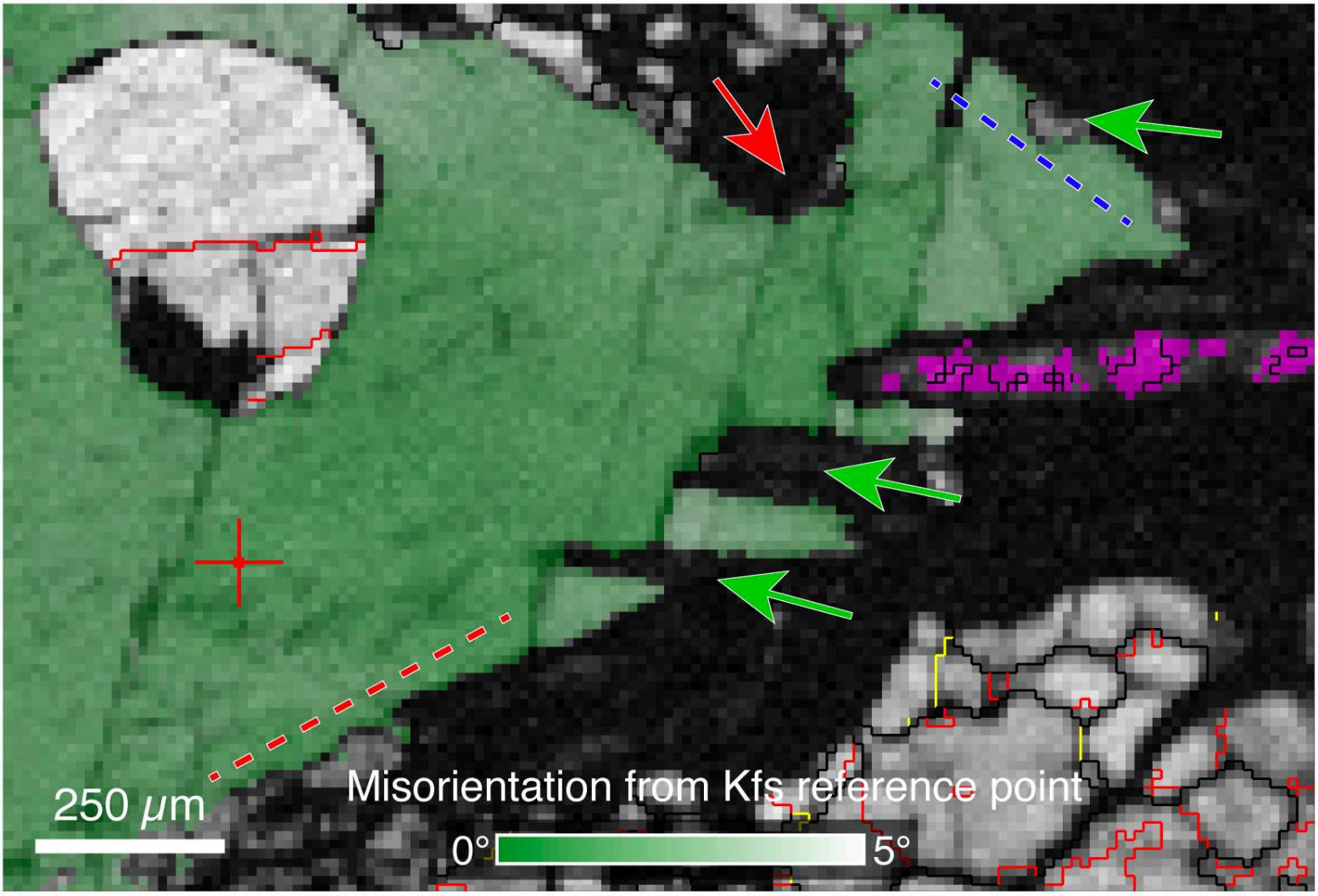

Sub-grain boundary (> 5°)

Grain boundary (> 10°)

Dauphine twin (60°)

Biotite

Quartz

Reference point:

Fig. 10

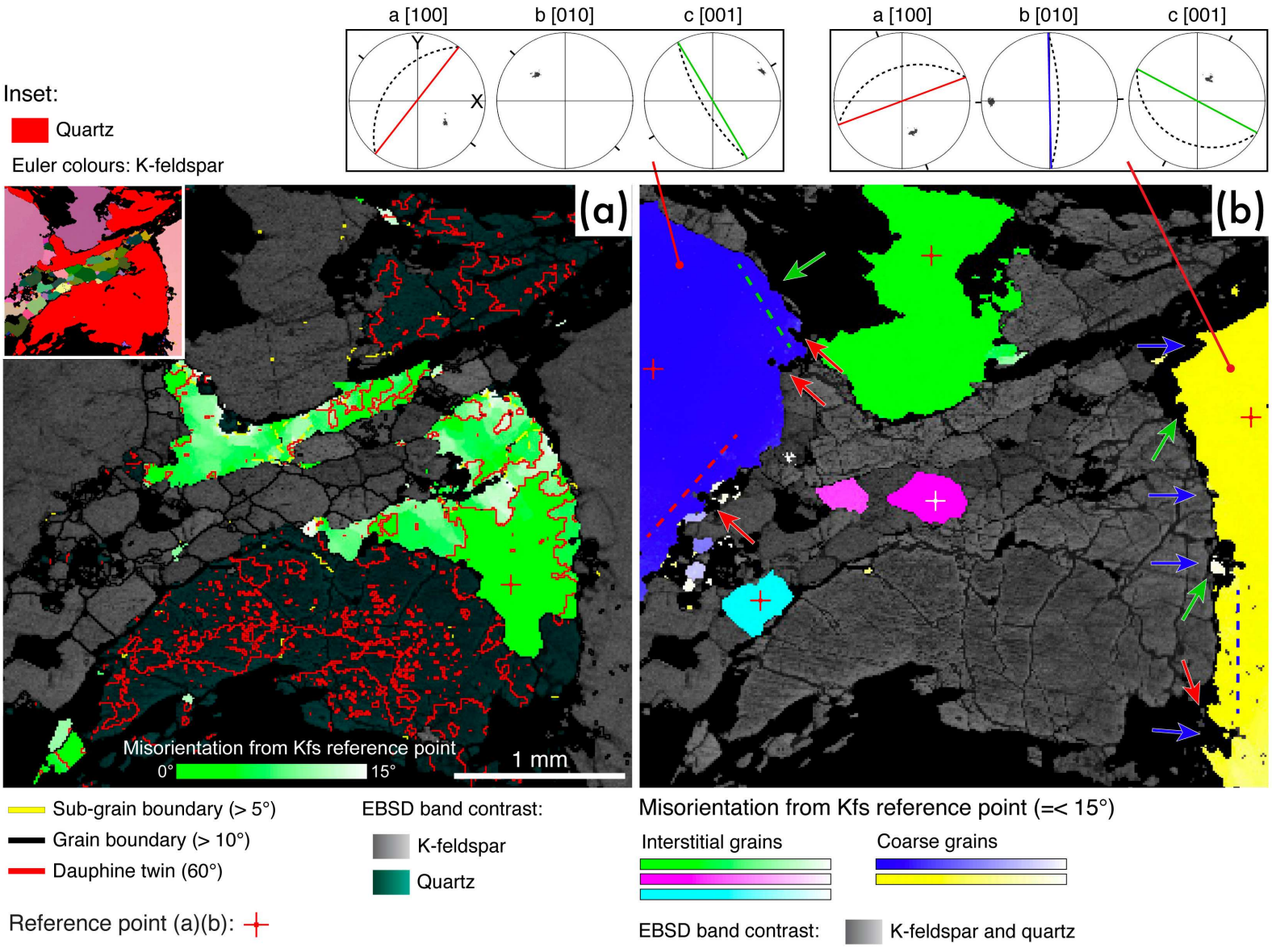
a [100]
b [010]
c [001]
Y
X
a [100]
b [010]
c [001]
Inset:
Quartz
Euler colours: K-feldspar
(a)
(b)
Misorientation from Kfs reference point
0°
15°
1 mm
Sub-grain boundary (> 5°)
Grain boundary (> 10°)
Dauphine twin (60°)
Reference point (a)(b):
EBSD band contrast:
K-feldspar
Quartz
Misorientation from Kfs reference point (=< 15°)
Interstitial grains
Coarse grains
EBSD band contrast:
K-feldspar and quartz

Fig. 11

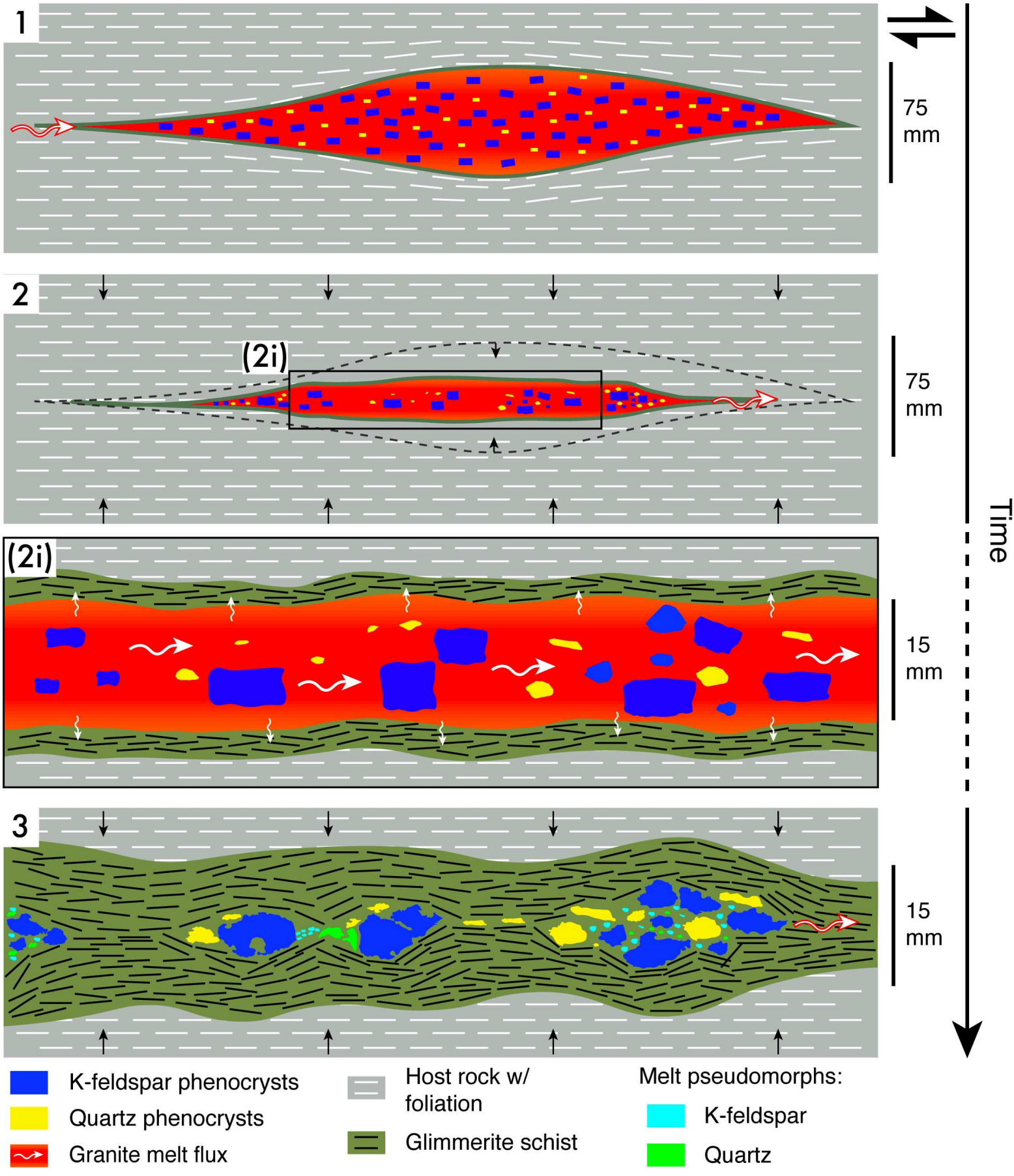
1
75 mm
2
(2i)
75 mm
(2i)
15 mm
3
15 mm
Time
K-feldspar phenocrysts
Quartz phenocrysts
Granite melt flux
Host rock w/ foliation
Glimmerite schist
Melt pseudomorphs:
K-feldspar
Quartz

Table 1: Selected electron microprobe data on multiple minerals for glimmerite schist present in GDSZ.

Sample	**Glimmerite schist (GD1606)**		
Mineral	*Bt*	*Kfs*	*Pl*
SiO_2 wt%	35.73	63.75	67.10
TiO_2	2.55	–	–
Al2O3	17.78	18.78	20.36
V_2O_3	0.04	–	–
Cr_2O_3	–	–	–
FeO_{total}	17.69	0.04	–
NiO	–	–	–
MnO	0.10	–	–
MgO	11.58	–	–
CaO	–	–	0.62
Na_2O	0.20	1.46	11.43
K_2O	9.71	14.18	0.11
P_2O_5	–	0.14	0.13
SO_3	–	–	–
Cl	0.41	0.04	–
F	0.59	–	–
O	-0.34	0.01	0.00
H_2O	3.93	0.00	0.00
Total	*99.97*	*98.41*	*99.73*

Mineral abbreviation follow Whitney & Evans (2010). (–): Below detection limit. The complete dataset is available in Table S1.

Table 2: Representative REE composition of K-feldspar grains from GDSZ and non-GDSZ published data from multiple locations.

Sample/ *Mineral*	**Gough Dam shear zone**			**Compilation of published Kfs composition (non-GDSZ)**			
	Glimmerite schist (GD1606)		Granitic lens (GD1620A)	Gneiss[(1)]	Pegmatite[(2)]	Migmatite[(3)(4)]	
	Coarse grains	*Interstitial*					
La	5.755	9.139	2.072	60.759	6.013	10.684	4.869
Ce	3.830	8.450	1.206	25.775	3.002	6.982	1.558
Pr	2.963	6.703	0.879	- -	1.638	5.065	0.472
Nd	2.103	6.915	0.654	–	0.910	2.276	0.821
Sm	1.358	6.189	0.601	1.142	0.696	1.554	3.027
Eu	2.284	20.462	4.352	24.156	6.767	32.682	34.547
Gd	0.829	8.146	0.563	- -	0.538	0.905	0.061
Dy	0.663	7.748	0.585	- -	0.585	0.569	0.043
Er	0.885	6.713	0.869	- -	0.731	0.625	0.029
Yb	1.006	4.950	1.205	0.068	0.944	0.621	0.036
Lu	1.053	4.297	0.951	- -	1.098	0.407	0.041

REE values were normalised using McDonough & Sun (1995) chondritic values. (1) Granodiorite gneiss porphyroblasts (Bingen *et al.*, 1990); (2) Pegmatite (Larsen, 2002); (3) Peraluminous migmatite leucosome (Bea *et al.*, 1994); (4) Kfs-rich evolved leucosome (Carvalho *et al.*, 2016). Mineral abbreviation follow Whitney & Evans (2010). The complete dataset is available in Table S2. (–): Below detection limit; (- -): Not available.